Available online at www.sciencedirect.com
ScienceDirect
Acta Materialia 58 (2010) 4458–4477
Acta MATERIALIA
www.elsevier.com/locate/actamat

Void initiation in fcc metals: Effect of loading orientation and nanocrystalline effects

Eduardo M. Bringa [a], Sirirat Traiviratana [b], Marc A. Meyers [b,*]

[a] CONICET, Instituto de Ciencias Básicas, Universidad Nacional de Cuyo, Mendoza 5500, Argentina
[b] University of California, San Diego, La Jolla, CA 92093, USA

Received 26 January 2010; received in revised form 16 April 2010; accepted 26 April 2010
Available online 1 June 2010

Abstract

It is shown, through molecular dynamics simulations, that the emission and outward expansion of special dislocation loops, nucleated at the surface of nanosized voids, are responsible for the outward flux of matter, promoting their growth. Calculations performed for different orientations of the tensile axis, [0 0 1], [1 1 0] and [1 1 1], reveal new features of these loops for a face-centered cubic metal, copper, and show that their extremities remain attached to the surface of voids. There is a significant effect of the loading orientation on the sequence in which the loops form and interact. As a consequence, the initially spherical voids develop facets. Calculations reveal that loop emission occurs for voids with radii as low as 0.15 nm, containing two vacancies. This occurs at a von Mises stress approximately equal to $0.12G$ (where G is the shear modulus of the material), and is close to the stress at which dislocation loops nucleate homogeneously. The velocities of the leading partial dislocations are measured and found to be subsonic ($\sim$1000 m s^{-1}). It is shown, for nanocrystalline metals that void initiation takes place at grain boundaries and that their growth proceeds by grain boundary debonding and partial dislocation emission into the grains. The principal difference with monocrystals is that the voids do not become spherical and that their growth proceeds along the boundaries. Differences in stress states (hydrostatic and uniaxial strain) are discussed. The critical stress for void nucleation and growth in the nanocrystalline metal is considerably lower than in the monocrystalline case by virtue of the availability of nucleation sites at grain boundaries (von Mises stress $\sim 0.05G$). This suggests a hierarchy of nucleation sites in materials, starting with dispersed phases, triple points and grain boundaries, and proceeding with vacancy complexes up to divacancies.

Keywords: Molecular dynamics; Dislocations; Copper; Nanostructure; Voids

1. Introduction

Ductile metals fail by the nucleation, growth and coalescence of voids, leading to the classical dimpled fracture, in contrast to brittle materials, where fracture is governed by crack nucleation, growth and coalescence. There has been intense inquiry, of experimental, analytical and computational nature, on the formation of voids during plastic deformation in tension, since the first report by Tipper [1] in 1948, which revealed the classic sequence of void nucleation, growth and coalescence. Indeed, this is a central problem in Materials Science and Engineering, since it is intimately associated with ductile failure of materials. In 1964, Chin et al. [2] compared polycrystalline and monocrystalline aluminum pulled in tension, and demonstrated that for the monocrystalline case the absence of void nucleation at particle sites led to fracture by "rupture" with a 100% reduction in area. However, earlier work by Rosi and Abrahams [3] demonstrated, for Al and Cu monocrystals, that there were voids in the neck region. Their formation was wrongly attributed to vacancy condensation, as will be shown here. The literature on the mechanics of void growth and coalescence is abundant, and the papers by Needleman and co-workers (e.g. [4,5]), Tvergaard and Hutchinson [6], Pardoen and Hutchinson [7], Gurson [8]

* Corresponding author. Tel.: +1 858 534 4719; fax: +1 858 534 5698.
E-mail address: mameyers@ucsd.edu (M.A. Meyers).

1359-6454/$36.00
doi:10.1016/j.actamat.2010.04.043

and McClintock [9] are noteworthy. A complete account on the nucleation, growth and coalescence of voids is given by Dodd and Bai [10].

In spite of the fact that ductile failure is an extensively investigated phenomenon, there is little information on the dislocation mechanisms of the homogeneous void initiation process, and it is often assumed that it is governed by the diffusion of vacancies towards a central point, creating and nourishing a void. This is due to the fact that in "engineering alloys" there is an ample supply of initiation sites, which in most cases are inclusions, precipitates and grain boundaries.

The first proposal for the homogeneous initiation of voids (not quantitatively expressed) was by Rosi and Abrahams [3], and was based on diffusion. One of the most rapid diffusion mechanisms is "pipe" diffusion, in which vacancies migrate along the dislocation line, and Cuitiño and Ortiz [11] developed a specific mechanism for this mode. Conventional plastic deformation at a conservative strain rate $10^{-2}\,s^{-1}$ will lead to a failure time of 10^2 s assuming a strain of 1 (using the activation energy for grain-boundary diffusion from Surholt and Herzig [12]). Failure is typically characterized by voids with radii ranging in the micrometers. However, the time predicted by Cuitiño and Ortiz [11] for voids to reach 0.1 μm at 300 K is much longer ($\sim 10^{10}$ s). Even at 600 K, voids cannot grow to a size equal to 0.1 μm in 10^2 s. Thus, vacancy diffusion, which is the principal mechanism of void growth in creep fracture, as treated by Raj and Ashby [13], cannot be the operating mechanism in conventional plastic deformation.

It is intriguing that dislocation-based models for the homogeneous initiation and growth of voids have only received scant attention in the literature. In one mechanism, proposed by Stevens et al. [14], the void is a sink for dislocations. A second mechanism, proposed by Meyers and Aimone [15], consists of intersecting dislocations diverging from a point. Both mechanisms are physically implausible. There is also a vague mention to dislocations in Broek [16], without any specific model being proposed. To treat porosity and plasticity in radiation-damaged materials, Wolfer [17] proposed void growth by emission of prismatic loops, and this mechanism has been adopted by others [18]. In 2004, Lubarda et al. [19] postulated that voids grew by the emission of both prismatic and shear loops, in analogy with the Ashby [20,21] mechanism for the generation of geometrically necessary dislocations in the deformation of plastically inhomogeneous materials. This mechanism has been supported by recent molecular dynamics calculations [22,23] on the [0 0 1] tensile direction, and this model [19] fits the simulation results extremely well. Marian et al. [24,25] carried out quasi-continuum (QC) calculations which showed the formation of shear loops in aluminum subjected to simple shear, with loops emerging from a void surface (Figs. 2 and 4 from Ref. [25]). Dávila et al. [26] demonstrated, using molecular dynamics (MD) simulations, that the emission of loops was responsible for the collapse of voids. The MD simulations of Zhu et al. [27] showed that shear loops are the principal agents for void growth during release of a shocked Al sample. The QC analysis by Marian et al. [24,25] was extended to a body-centered cubic (bcc) metal (Ta) recently [28], essentially confirming the generation of loops at the surface of an expanding void. There have also been a number of MD efforts modeling the growth of voids, focusing on details other than dislocation activity [29–34]. Rudd [35] observed, in detailed MD calculations, the formation of loops in both face-centered cubic (fcc) and bcc metals. Zhao et al. [36] modeled a monocrystal with cylindrical voids and observed the emission of shear loops.

The postulation and observation of loops forming around rigid particles in metals subjected to plastic deformation is not new. For the case of plastic deformation of metals containing rigid particles, a problem somewhat akin to the growth of voids, Seitz [37] and Brown [38] postulated prismatic loops forming at the interface between a rigid particle and matrix. In related work, Ashby [20,21] discussed both shear and prismatic loops observed by transmission electron microscopy. Hirsch [39] assumed that shear loops formed first and underwent a double cross slip process in the process of traversing a rigid particle, leaving behind a prismatic loop. He observed arrays of these loops in copper. In a later paper [40] (Fig. 15, loop marked A) he shows a shear loop very similar to one of our MD observations. Table 1 of Ref. [40] analyzes the various possibilities, and includes shear loops. There are related simulation, models and experimental results which also point towards void plasticity mechanisms involving shear loops. Silcox and Hirsch [41] analyzed the dislocations that form the boundaries of stacking fault tetrahedra in gold. These tetrahedra had sizes of approximately 35 nm. Later, Humphreys and Hirsch [42] analyzed copper containing small alumina particles and observed the formation of prismatic loops by a cross-slip mechanism. This study involved primarily the interaction of existing dislocations with rigid particles. More recently, Uberuaga et al. [43] observed the direct transformation of vacancy voids to stacking fault tetrahedra by molecular dynamics.

The goals of the current investigation are (i) to establish the effect of loading orientation on the formation of dislocations responsible to grow the void, (ii) to determine the minimum pre-existing void size around which dislocations nucleate and promote growth, and (iii) to ascertain the role of grain boundaries as favorable nucleation sites in polycrystals, as recently shown [19,23,34], and as discussed in simulations of fracture of polycrystalline samples [44–46].

2. Computational methods

The molecular dynamics LAMMPS (large-scale atomic/molecular massively parallel simulator) [47] code was used in this investigation. For the fcc copper structure, the embedded atom method (EAM) potential [48] by Mishin et al. [49] was used. The number of atoms was varied from 10^4 to 10^7, and calculations were performed on parallel PCs

and on supercomputers at the San Diego and Texas Super Computer Centers.

The single crystal copper domain was a cube with a spherical void at the center. Periodic boundaries were applied in all directions. The different domains were subjected to uniaxial strain along [1 0 0], [1 1 0] and [1 1 1]. All simulations for monocrystals were done at an initial temperature of 150 K and strain rate of $10^8\ s^{-1}$ for times up to 2 ns, corresponding to 20% volume strain. For the polycrystals, they were carried out at a strain rate of $10^9\ s^{-1}$ and an initial temperature of 5 K. All samples were equilibrated to reach zero pressure and the desired initial temperature. Loading was carried out without any temperature control, to capture temperature effects related to plasticity. Visualization of stacking faults, partial dislocations and free surfaces was conducted with a filter using the centrosymmetry parameter [50].

3. Results and discussion

This section is divided into three parts: effect of loading orientation; effect of void size; and void initiation in poly(nano)crystalline metals.

3.1. Effect of loading orientation on dislocation evolution

The calculations were performed for voids with 2 nm radius and three orientations of the tensile axis: [1 0 0], [1 1 0] and [1 1 1]. These are the corners of the stereographic triangle. They have the following number of slip systems with highest Schmid factor:

[1 0 0]	eight slip systems
[1 1 0]	four slip systems
[1 1 1]	six slip systems.

Loops emission occurs, as postulated by Lubarda et al. [19], from the line corresponding to the intersection of the slip plane making an angle of 45° with the surface of the void and the void surface. This orientation maximizes the shear stress, as was shown by Lubarda et al. [19] and Traiviratana et al. [22]. The traces of two slip planes are illustrated in Fig. 1 for a [1 1 0] loading direction (marked by arrows). The 45° angles with the surface are marked, and they make an angle of 109.47°. The sequence of shear loop initiation and expansion is demonstrated here for the three loading orientations, [1 1 0], [1 0 0] and [1 1 1], in order of complexity.

3.1.1. Load application direction [1 1 0]

This loading orientation provides the simplest dislocation configuration. Fig. 2 shows the sequence of expansion of a shear loop for [1 1 0] loading. Only the leading partial dislocation is emitted during the computational time (limited by the domain size), and the (1 1 1) slip plane, as expected, makes an angle of 45° with the surface of the spherical void (radius = 2 nm). This angle is shown in

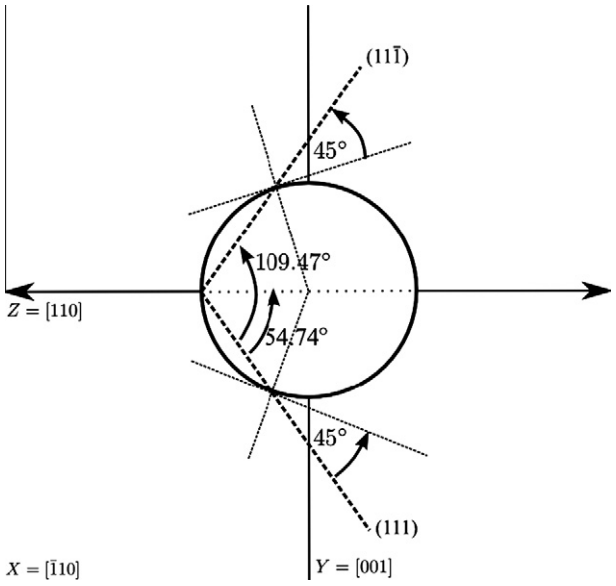

Fig. 1. Schematic showing traces of two slip planes intersecting a void at 45°. The loading axis ([1 1 0]) is marked by arrows.

Fig. 2d. The expansion of the shear loop is shown in Fig. 2b. The expansion of the loop proceeds as shown in Fig. 2a–c. The loop does not detach itself from the void, nor does it circumnavigate it. This "attachment" condition is necessary to create the shear at a portion of the void surface. Complete shear of the void would not produce its volume change. The loop acquires a heart shape (Fig. 2c). In Fig. 2d a second loop is shown. For this direction of loading, the application of Schmid equation predicts four slip systems with highest Schmid factors (=0.408):

$$\begin{aligned}(1\,1\,1) &\rightarrow [0\,1\,\bar{1}]\\ &\rightarrow [\bar{1}\,0\,1]\\ (\bar{1}\,\bar{1}\,1) &\rightarrow [0\,\bar{1}\,\bar{1}]\\ &\rightarrow [1\,0\,1]\end{aligned}$$

Fig. 2d shows that the two slip planes, (1 1 1) and ($\bar{1}\,\bar{1}$ 1), do indeed make an angle of 54.7° with the loading axis (and an angle of 109.4° between them).

3.1.2. Load application direction [1 0 0]

For this orientation (sequence shown in Fig. 3), a cooperative growth of partial dislocation loops is observed. The reactions were analyzed in detail by Traiviratana et al. [22] and will therefore not be reproduced here. There are eight systems with the highest Schmid factor of 0.408. A biplanar shear loop emerges from the surface of the void, on planes (1 $\bar{1}\,\bar{1}$) and ($\bar{1}\,\bar{1}\,\bar{1}$), marked in Fig. 3b. These planes and the respective ⟨1 1 0⟩ define the maximum Schmid factor orientations. The two leading partial dislocations advance, moving away from the void. The trailing partials are subsequently formed. At the intersection of (1 $\bar{1}\,\bar{1}$) and ($\bar{1}\,\bar{1}\,\bar{1}$), the dislocation formed by the reaction of the leading partials $\left(\frac{a}{6}[\bar{1}\,\bar{2}\,1] - \frac{a}{6}[\bar{1}\,\bar{1}\,2] \Rightarrow \frac{a}{6}[0\,\bar{1}\,\bar{1}]\right)$ is sessile. It is cancelled by the one forming by the reaction of the trailing

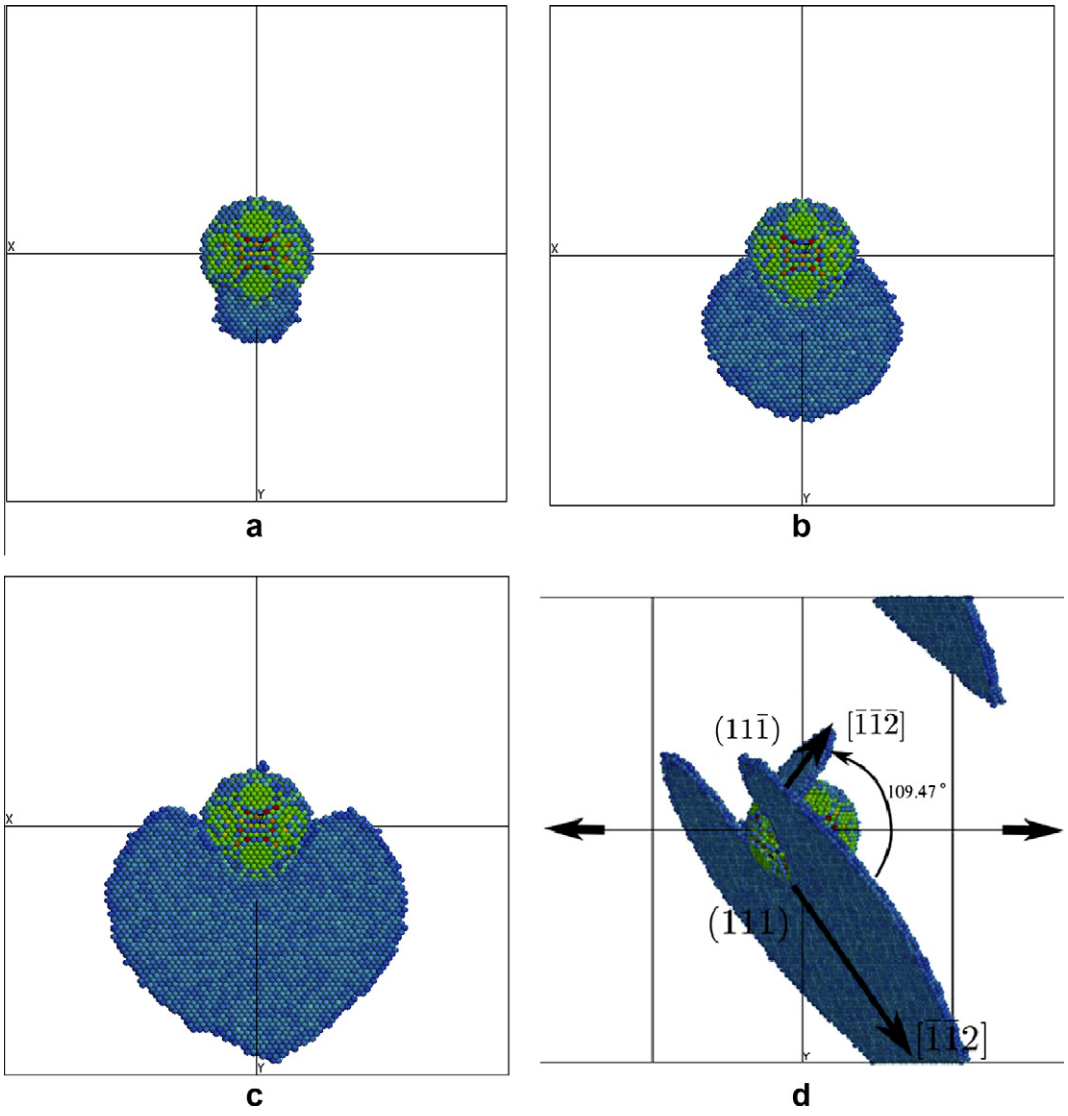

Fig. 2. Sequence of shear loop nucleation and growth for the [1 1 0] loading direction. Note the directions and planes in (d) as well as the second loop forming (the loading direction is perpendicular to plane of paper for (a–c), and is marked in (d)). Only non-fcc atoms are shown, thanks to a centrosymmetry parameter [50] filter. Atoms in the stacking fault are light blue.

partials $\left(\frac{a}{6}[1\,\bar{1}\,2]-\frac{a}{6}[1\,\bar{2}\,1]\Rightarrow\frac{a}{6}[0\,1\,1]\right)$, also sessile. Upon further loading, additional loops form on other planes (Fig. 3c and d).

3.1.3. Load application direction [1 1 1]

The growth sequence is shown in Fig. 4. Similar to [1 1 0] and [1 0 0], the loading axis is perpendicular to the plane of the paper. One loop is initially generated, closely followed by two loops on different planes. The leading partials connect at the intersection of the planes, forming a triplanar loop. As the shear loops expand by the glide of the leading partial dislocations, the trailing partials form the network shown in Fig. 4c.

Fig. 5a shows the schematic of the three slip planes with the leading and trailing partial dislocations as well as the stacking faults shown. A more detailed MD view of the expansion of the triplanar loops, shaped like a parachute, is seen in Fig. 5b. The three slip planes are $(1\,\bar{1}\,\bar{1}),(\bar{1}\,\bar{1}\,1)$ and $(\bar{1}\,1\,\bar{1})$, and the slip directions within each plane are indicated. Thus, the three slip planes are simultaneously and cooperatively activated. The fact that the trailing partials nucleate at the intersection of the planes suggests that this is an energetically favorable point. Schmid factor computations predict the following six slip systems with the highest Schmid factors (=0.272) involving the three planes:

$$\begin{aligned}(\bar{1}\,1\,\bar{1}) &\rightarrow [0\,1\,1]\\ &\rightarrow [\bar{1}\,\bar{1}\,0]\\ (\bar{1}\,\bar{1}\,1) &\rightarrow [0\,1\,1]\\ &\rightarrow [1\,0\,1]\\ (1\,\bar{1}\,\bar{1}) &\rightarrow [1\,0\,1]\\ &\rightarrow [\bar{1}\,\bar{1}\,0]\end{aligned}$$

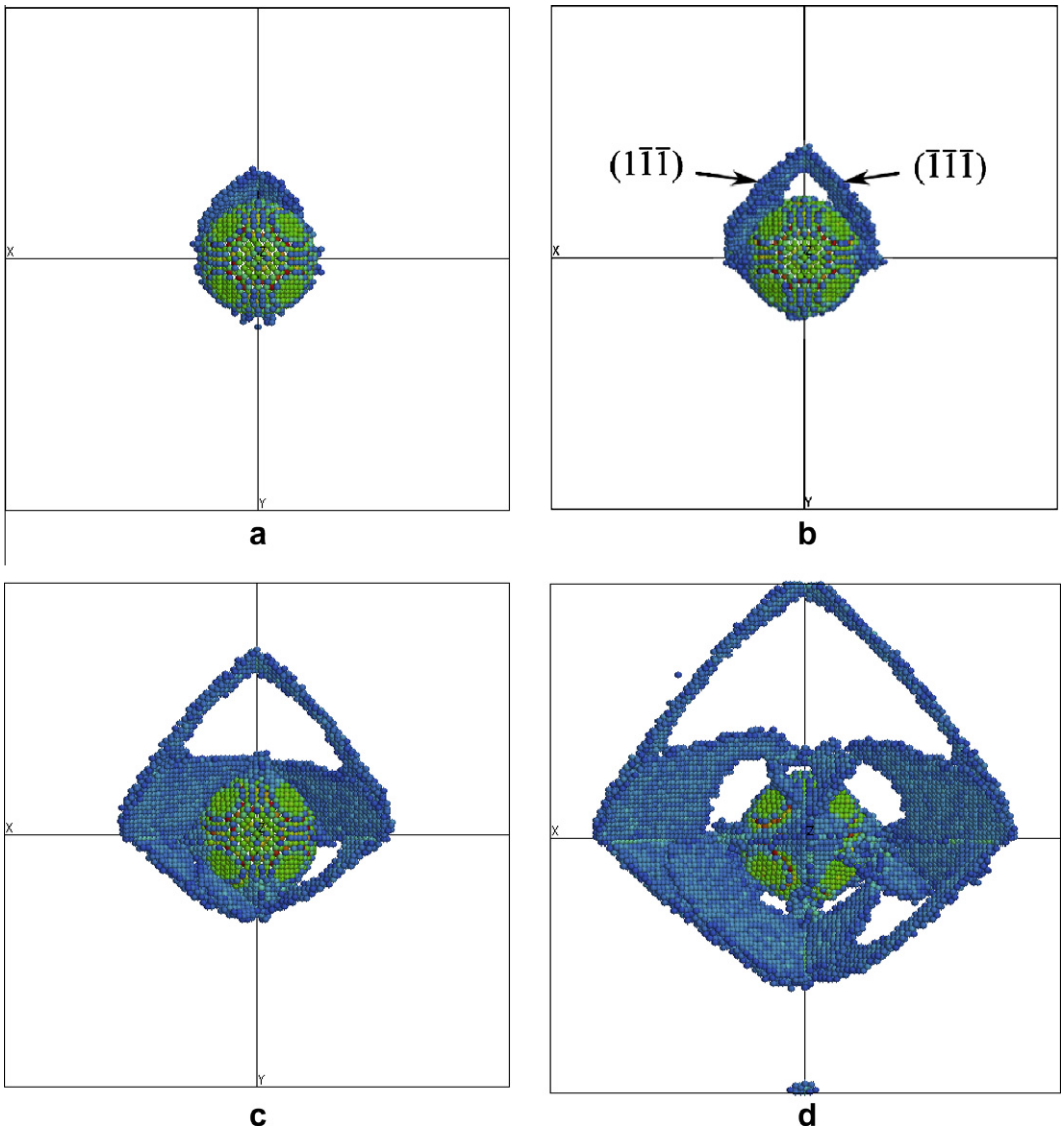

Fig. 3. Sequence of loop nucleation and growth for loading along [1 0 0] (the loading direction is perpendicular to plane of paper). Note the two loops forming on (1 1 1) and $(\bar{1}\,\bar{1}\,\bar{1})$, reacting and forming a biplanar loop.

The evolution of the dislocation configuration is analyzed in detail here. First, a small loop is nucleated on the surface of the void and glides along $(\bar{1}\,\bar{1}\,1)$ (Fig. 6a). When the $(\bar{1}\,\bar{1}\,1)$ intersects the $(\bar{1}\,1\,\bar{1})$ and $(1\,\bar{1}\,\bar{1})$ positioned such that they make 45° with the void surface, these planes give rise to two partials. In Fig. 6b the dislocations are represented in the three $(\bar{1}\,1\,\bar{1})$, $(\bar{1}\,\bar{1}\,1)$ and $(1\,\bar{1}\,\bar{1})$ planes, which are projected on a single surface for clarity. Four of the six slip systems are represented by the three planes and two intersections in Fig. 6:

$(\bar{1}\,1\,\bar{1})[0\,1\,1]$

$(\bar{1}\,\bar{1}\,1)[0\,1\,1]$

$(\bar{1}\,\bar{1}\,1)[1\,0\,1]$

$(1\,\bar{1}\,\bar{1})[1\,0\,1]$

The intersection of $(\bar{1}\,1\,\bar{1})$ and $(\bar{1}\,\bar{1}\,1)$ is [0 1 1]; that of $(\bar{1}\,\bar{1}\,1)$ and $(1\,\bar{1}\,\bar{1})$ is [1 0 1]. Fig. 6b shows the leading partials only, whereas Fig. 6c shows the configuration after the trailing partials were emitted. In the middle plane, $(\bar{1}\,\bar{1}\,1)$, the Burgers vector of the partial dislocation is inferred to be $b_{p1} = a/6[1\,1\,2]$. The perfect dislocations [1 0 1] and [0 1 1], with Burgers vectors aligned with the intersections of the planes, can be decomposed into partials in $(\bar{1}\,\bar{1}\,1)$ along the following reactions, shown in Fig. 6b:

$$a/2[1\,0\,1] \rightarrow b_{p1} + b'_{p2} \rightarrow a/6[1\,1\,2] + a/6[2\,\bar{1}\,1]$$

$$a/2[0\,1\,1] \rightarrow b_{p1} + b_{p2} \rightarrow a/6[1\,1\,2] + a/6[\bar{1}\,2\,1]$$

In $(\bar{1}\,1\,\bar{1})$ and $(1\,\bar{1}\,\bar{1})$, the leading partials are, respectively, $b_{p5} = a/6[1\,2\,1]$ and $b_{p3} = a/6[2\,1\,1]$. The perfect dislocations in these two planes with Burgers vectors along the intersection with $(\bar{1}\,\bar{1}\,1)$ decompose into partials as:

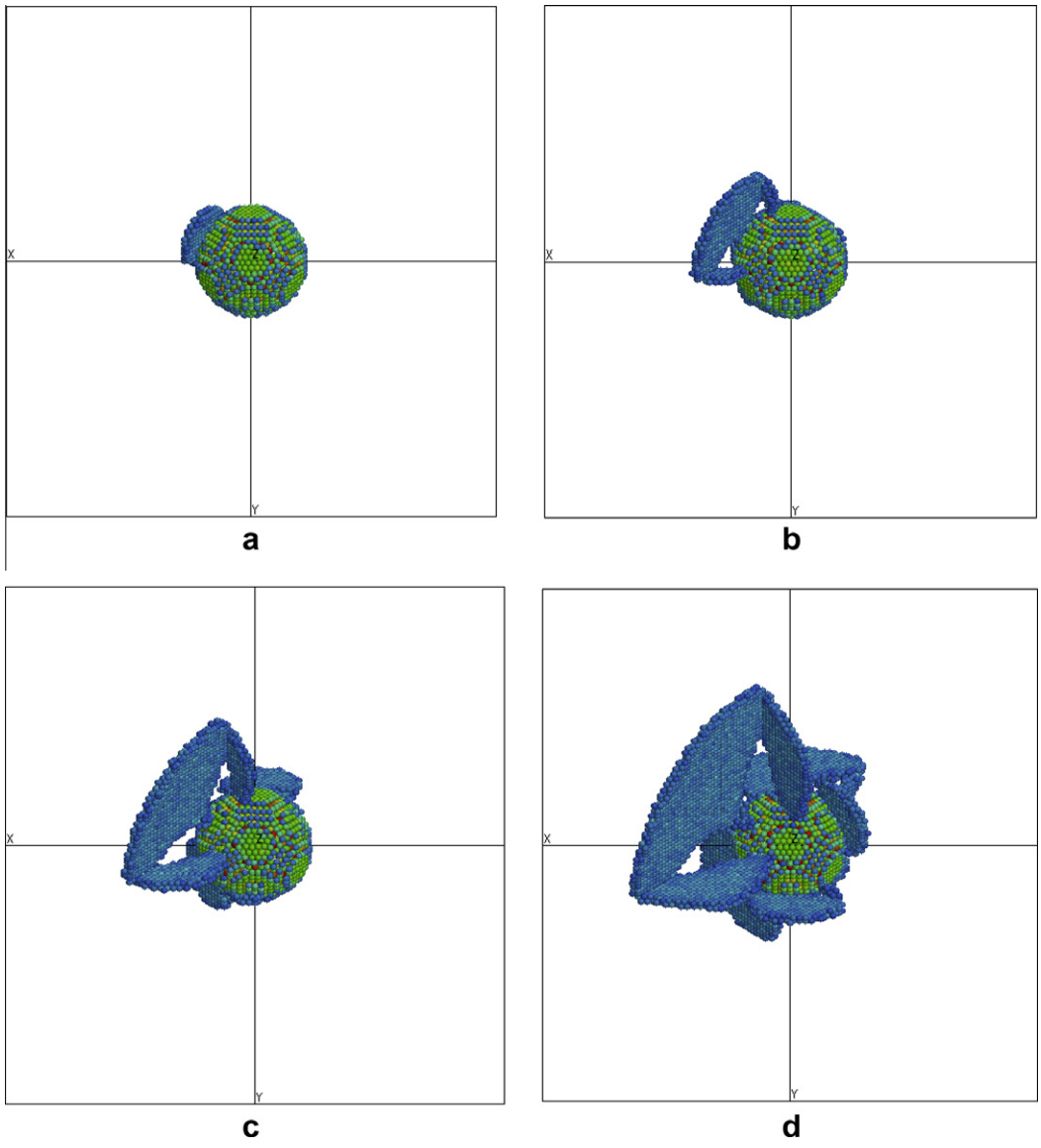

Fig. 4. Sequence of loop nucleation and growth for loading along [1 1 1] (the loading direction perpendicular to the plane of paper). Note the formation of loops on three planes in (b).

$$a/2[0\,1\,1] \rightarrow a/6[1\,2\,1] + a/6[\bar{1}\,1\,2] \quad (1)$$

$$a/2[1\,0\,1] \rightarrow a/6[2\,1\,1] + a/6[1\,\bar{1}\,2] \quad (2)$$

The trailing dislocations on $(\bar{1}\,\bar{1}\,1)$ are $b_{p2} = [\bar{1}\,2\,1]$ on the left-hand side and $b'_{p2} = a/6[2\,\bar{1}\,1]$ on the right-hand side. This is a unique configuration that will be discussed later. The leading and trailing partials react at the intersection of the slip planes. In an identical manner to the biplanar loop analysis [22], we need to incorporate the direction of the dislocation line into the analysis. We assume a clockwise line orientation for both cases. For $(\bar{1}\,\bar{1}\,1)$ and $(1\,\bar{1}\,\bar{1})$ the Burgers vectors of the reaction products of the leading and trailing dislocations are, respectively:

$$b_{rl} = b_{p1} + b_{p3} = a/6[1\,1\,2] + (-)a/6[2\,1\,1] = a/6[\bar{1}\,0\,1] \quad (3)$$

$$b_{rt} = b'_{p2} + b_{p4} = a/6[2\,\bar{1}\,1] + (-)a/6[1\,\bar{1}\,2] = a/6[1\,0\,\bar{1}] \quad (4)$$

b_{rl} and b_{rt} are sessile dislocations. The $(-)$ sign is used to account for the opposite sense in the dislocation lines at the intersection (using the right hand/finish start, or RHFS, convention). The energy of a dislocation is given by $\sim Gb^2/2$. The energy criterion states that a dislocation reaction should lead to lower energy configuration and provides:

$$\frac{a^2}{6} + \frac{a^2}{6} = \frac{a^2}{3} > \frac{a^2}{18}$$

Thus, the reaction is energetically favorable. The trailing reaction product b_{rt} and the leading reaction product b_{rl} react:

$$b_{rl} + b_{rt} = a/6[\bar{1}\,0\,1] + a/6[1\,0\,\bar{1}] = 0$$

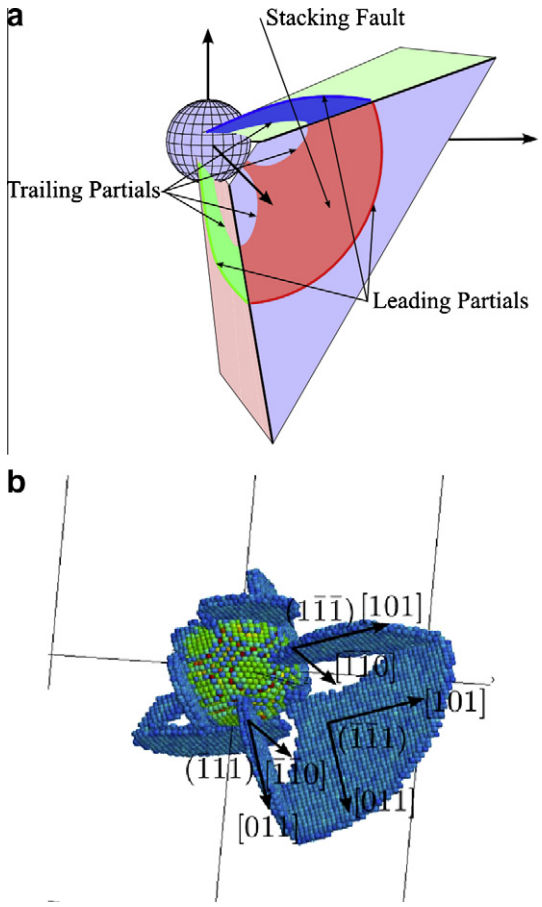

Fig. 5. Plane and directions labeled for the [1 1 1] loading direction: (a) schematic illustration and (b) MD simulation.

Thus, the two dislocations cancel each other and the perfect lattice is recomposed.

For $(\bar{1}\,\bar{1}\,1)$ and $(\bar{1}\,1\,\bar{1})$:

$$b_{rl} = b_{p1} + b_{p5} = a/6[1\,1\,2] + (-)a/6[1\,2\,1] = a/6[0\,\bar{1}\,1]$$
$$b_{rt} = b_{p2} + b_{p6} = a/6[\bar{1}\,2\,1] + (-)a/6[\bar{1}\,1\,2] = a/6[0\,1\,\bar{1}]$$

These are also sessile dislocations. The reactions are similarly energetically favorable. The trailing and leading reaction products, on their turn, generate:

$$b_{rl} + b_{rt} = a/6[0\,\bar{1}\,1] + a/6[0\,1\,\bar{1}] = 0$$

Similarly to the right-hand side, the two sessile dislocations cancel each other. An important question is: will b_{p2} and b'_{p2} react? If they react, the resulting dislocation could detach from the void surface.

$$b_{p2} + b'_{p2} = a/6[\bar{1}\,2\,1] + (-)a/6[2\,\bar{1}\,1] = a/2[\bar{1}\,1\,0]$$

This will entail an increase in energy, since:

$$\frac{a^2}{6} + \frac{a^2}{6} < \frac{a^2}{2}$$

There is another aspect: a perfect dislocation traveling through a faulted region would not bring it back to the perfect lattice. All of this precludes the reaction, thus the trailing partials remain attached to the surface of the void. This has an important bearing on the expansion of the void. The situation depicted in Figs. 5 and 6 is quite unique, because one single leading partial dislocation is followed by two complementary partials, one on each side. This enables slip on two directions but on a single plane, an apparent paradox.

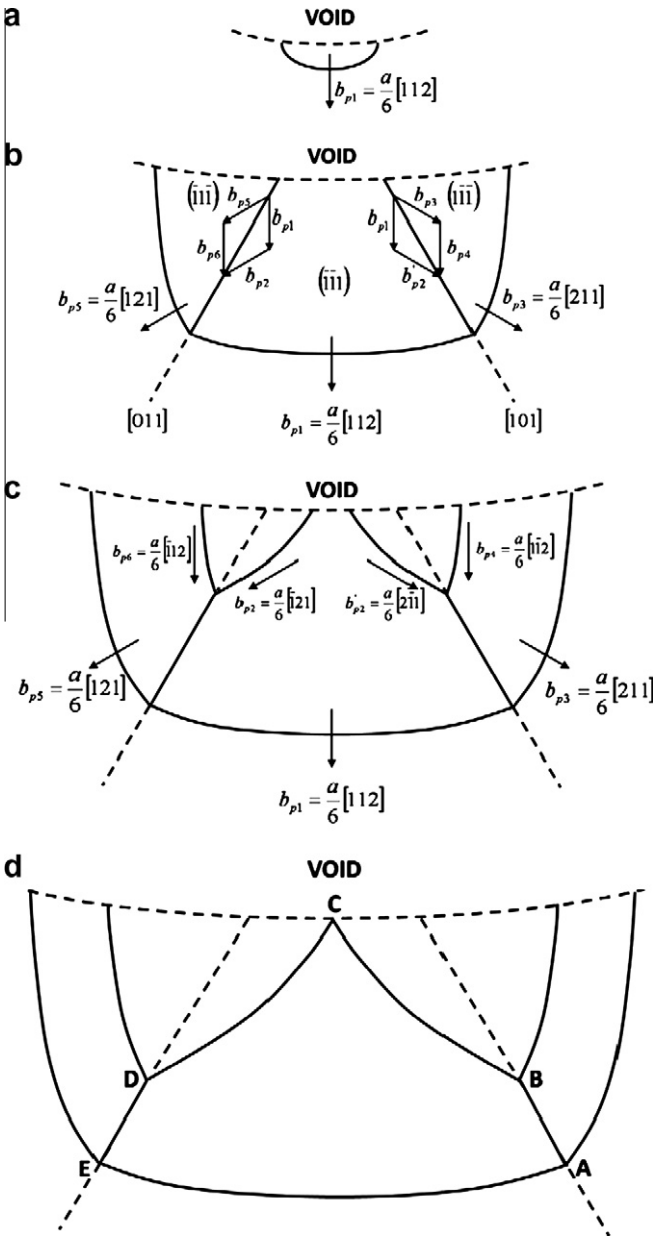

Fig. 6. Planar representation of dislocation activity on three $(1\,\bar{1}\,\bar{1})$, $(\bar{1}\,\bar{1}\,1)$ and $(\bar{1}\,1\,\bar{1})$ planes: (a) leading partial emitted in $(\bar{1}\,\bar{1}\,1)$; (b) leading partials along three planes; (c) leading and trailing partials emitted; (d) advanced configuration showing constriction along the [0 1 1] and [1 0 1] intersections and anchoring of trailing partials at the void surface (point C).

3.1.4. Stresses at the onset of growth

Fig. 7 shows the mean and von Mises stresses as a function of tensile strain for samples with 0.4% porosity ($\sim 7 \times 10^5$ atoms). The von Mises stresses vary linearly with

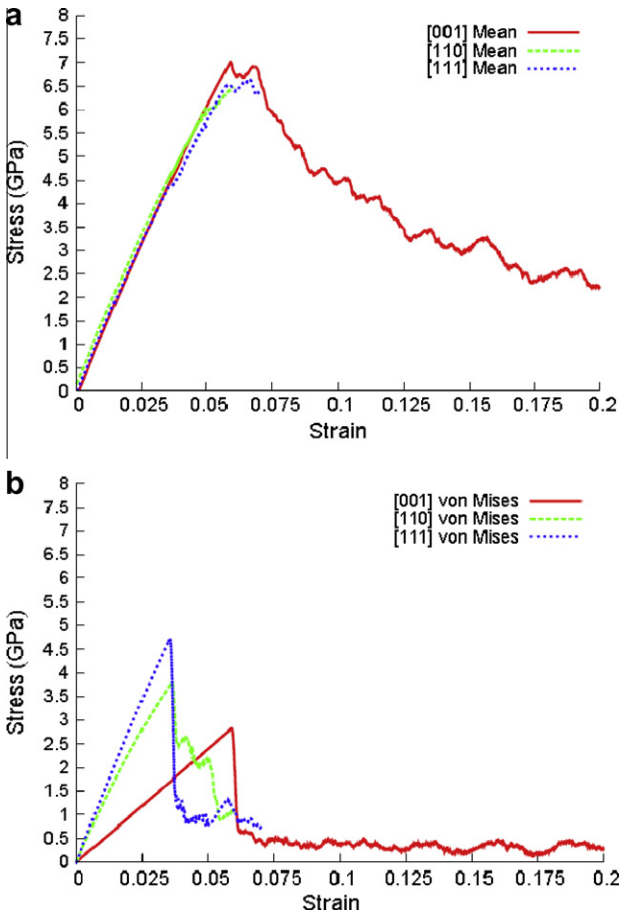

Fig. 7. Effect of void orientation on the strain–stress evolution: (a) hydrostatic (mean) stresses and (b) von Mises stresses.

strain until the maximum, and the slopes follow the relationship between elastic constants:

$$E_{[1\,0\,0]} < E_{[1\,1\,0]} < E_{[1\,1\,1]}$$

The experimental values of the elastic constants for copper give: $E_{[100]} = 66$ GPa, $E_{[110]} = 130$ GPa, $E_{[111]} = 191$ GPa. Using the values for the elastic constants of the Mishin potential [49], one obtains: $E_{[100]} = 67$ GPa, $E_{[110]} = 131$ GPa, $E_{[111]} = 193$ GPa. Thus, the values are very close. The values derived from Fig. 7(b) are ~15–25% smaller due to the presence of the void.

The mean stresses follow approximately the same trajectory for the three orientations. The von Mises stress (Fig. 7b) shows differences near the maximum. This defines the strain at which plasticity begins. As can be seen, [1 0 0] yields at a strain of ~6%, while the other two orientations yield at a strain of ~3.5%. We find von Mises stresses of 2.8, 3.8 and 4.75 GPa for loading along [1 0 0], [1 1 0] and [1 1 1] respectively. The lower yield stress for [1 0 0] is connected to the greater availability of slip systems (eight) with the highest Schmid factor (0.408), in comparison with four systems with a Schmid factor of 0.408 for [1 1 0] and six systems with a Schmid factor of 0.272 for [1 1 1]. Minich et al. [51] found a higher spall strength (inferred from VISAR pullback signals) for [1 0 0] monocrystals, in comparison with [1 1 0] and [1 1 1], which had approximately the same value. Thus, our current results contrast with macroscopic measurements. This could be related to different types of pre-existing defects in single crystal samples, which are not included in MD simulations. Luo et al. [52] have recently shown loading orientation effects in spall strength of single crystal Cu under shock and release conditions, using MD simulations. In their work the spall strength values near room temperature are 15.9, 15 and 16.6 GPa for loading along [1 0 0], [1 1 0] and [1 1 1] respectively, and strain rates around 10^{10} s^{-1}. The different ordering of the "strength" for different loading orientations compared to our results could be due to strain rate effects.

3.1.5. Growth and faceting of voids

Fig. 8 shows the growth of voids with initial radii of 2 nm under uniaxial strain loading, similarly to the voids shown in Sections 3.1.1–3.1.3. The strain rate was 10^8 s^{-1}. Stacking faults emitted from the void surfaces are seen for the three loading orientations. Faceting is strongest for [0 0 1] loading, and less pronounced for the other directions. Nevertheless, the voids lose their sphericity at fairly low deformation. This is corroborated by experimental results as discussed by Meyers et al. [23]. This faceting was previously observed and quantified by Seppälä et al. [31].

3.1.6. Dislocation velocities

One can extract dislocation velocities from the expansion of voids. This is of special interest since the existence of three regimes of dislocation velocities, subsonic, transonic and supersonic, has been a subject of conjuncture for close to 60 years, all the way back since the early work of Frank [53] and Eshelby [54], expanded by Weertman [55,56]. Gumbsch and Gao [57] carried out MD simulations in tungsten that showed the possibility of the three regimes. Tsuzuki et al. [58] obtained the three regimes of dislocation velocity (subsonic, transonic and supersonic) in copper using a Mishin potential [49]. MD simulations by Dávila et al. [26] of copper under shock compression also point to the existence of partial dislocation loops expanding at velocities exceeding the shear wave speed. This is illustrated in Fig. 9. In these simulations a shock wave was sent along [0 0 1] in Cu, represented by a Mishin potential [49], in a sample with 13.5 million atoms (~54 × 54 × 54 nm^3), with a void of 2 nm radius at its center. The presence of the void allowed nucleation of dislocations well below the HEL of this sample ($P_{sh} \sim 32$ GPa). At relatively low shock pressures ($P = 8.4$ GPa) the dislocation velocity is much lower than the bulk sound velocity ($\sim 0.3 C_0$). This velocity agrees with the results by Rudd [35] on dislocation velocity for a void in Cu under hydrostatic tension, at a fixed strain rate. At the higher pressure shock simulations by Dávila et al. [26], 21 GPa, the velocity of the partial loops (4.4 km s^{-1}) is considerably higher than

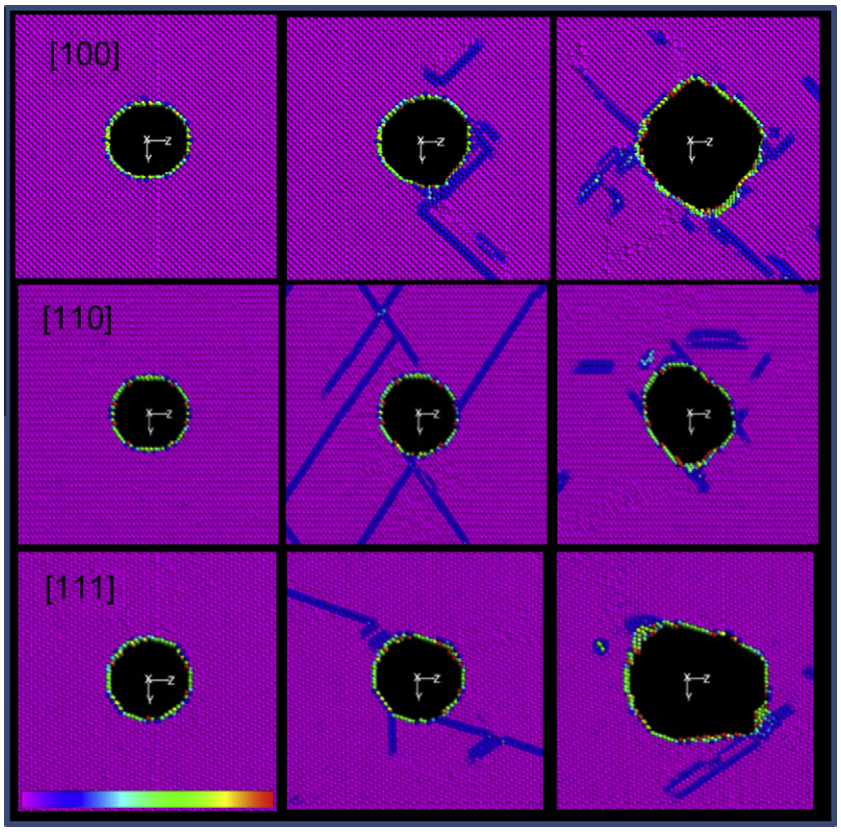

Fig. 8. Void growth and faceting for three loading orientations: [1 0 0], [1 1 0] and [1 1 1]. The time evolution is shown from left to right. Pink atoms are lattice atoms with high CSP; light blue atoms are stacking faults; green and red atoms are on the surface of void. A small slab with the plane perpendicular to the loading direction was taken. Strains: 4.8%, 5.2%, 6.1% for [1 0 0]; 3.4%, 4.4%, 5.3% for [1 1 0]; 3.4%, 3.9%, 6.8% for [1 1 1].

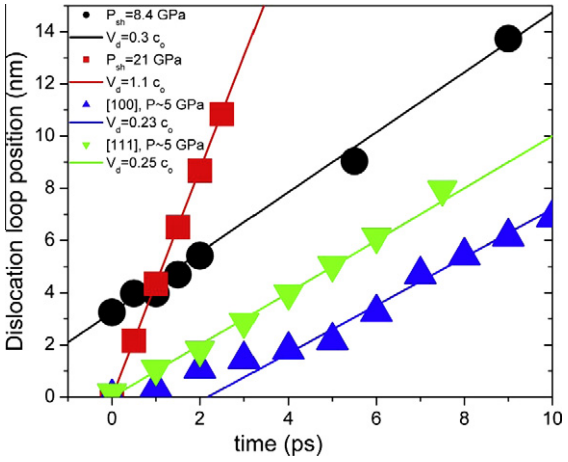

Fig. 9. Velocities of dislocations (expressed as a fraction of the bulk sound velocity, C_0) emanating from a collapsing void in a Cu specimen subjected to two shock pressures, 8.4 and 21 GPa (data from Dávila et al. [26]), and for an expanding void at $P \sim 5$ GPa.

the shear wave velocity (2.32 km s^{-1}) and even higher that the bulk sound velocity (~4 km s^{-1}). The current simulations, also included in the plot, show void expansion velocities of $0.25C_0$ for the loading along [1 1 1] and $0.23C_0$ for loading along [1 0 0]. We do note that the longitudinal sound velocities are approximately 4.2, 5 and 5.2 km s^{-1} along [0 0 1], [0 1 1] and [1 1 1] at zero pressure [59]. The dislocation velocity of ~4.4 km s^{-1} at a shock pressure of 21 GPa extracted from the data by Dávila et al. [26] corresponds to dislocation motion in the second transonic regime as presented by Tsuzuki et al. [58].

3.2. Void size effects

In order to investigate the applicability of the shear loop emission mechanism beyond the range of void sizes studied earlier [22,23], which had a minimum radius of 0.3 nm (13 vacancies), the initial void radius was decreased sequentially until a minimum of one vacancy (~0.1 nm). It is well known that metals have vacancies in equilibrium, because of the configurational entropy. A significant fraction of these vacancies exist as complexes (di, trivacancies, etc.). Thus, one would expect that they can act as nucleation sites for voids, in the absence of other defects, such as second-phase particles and grain boundaries.

Indeed, this is corroborated by the computations shown in Fig. 10. Fig. 10a shows the generation of partial loops (stacking faults bounded by a partial dislocation) in the absence of a void, by homogeneous nucleation as occurs in shock loading [60]. For the smallest void, containing only one vacancy, the loops still nucleate homogeneously in the box, independently of the void (Fig. 10b). For a

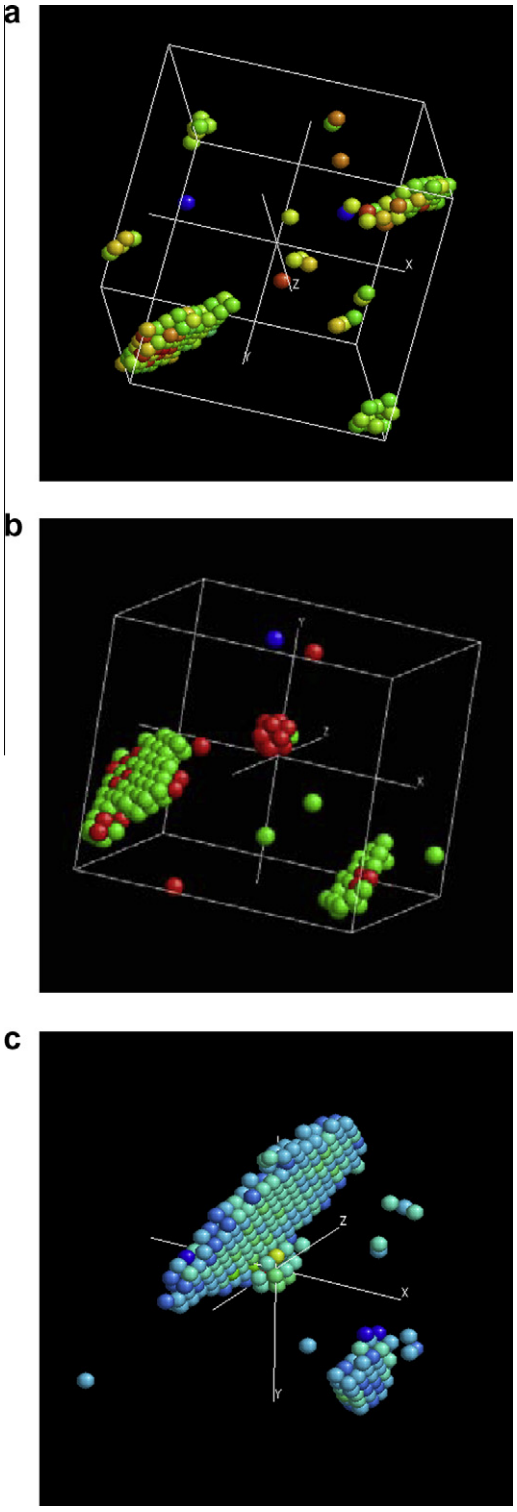

Fig. 10. Dislocation loop generation in the deformation of the sample with voids having radii of: (a) 0 nm (no vacancy), (b) 0.1 nm (one vacancy) and (c) 0.15 nm (two vacancies).

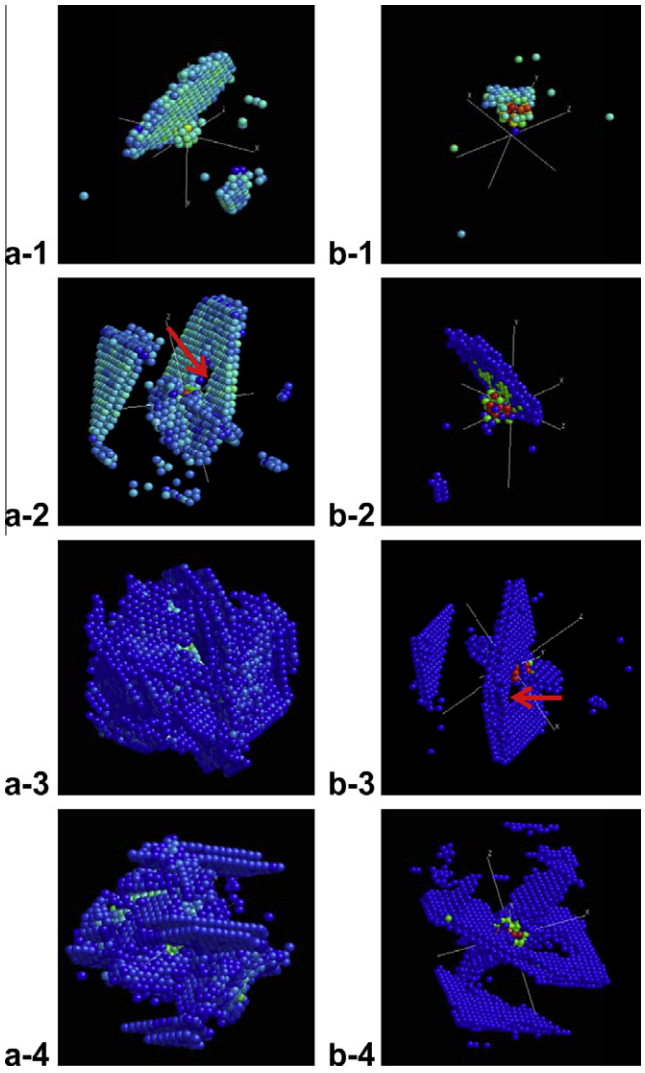

Fig. 11. Evolution of shear loops with increasing time for voids with (a) two (0.15 nm) and (b) four vacancies (0.2 nm). Loading direction: [1 0 0]. Note the trailing partial emission in (a-2) and (b-3) (arrows).

slightly larger void radius, 0.15 nm, containing two vacancies, the shear loop nucleates at this vacancy complex (Fig. 10c). The sequences of shear loop nucleation at increasing times for void radii of 0.15 (two vacancies) and 0.2 nm (four vacancies) are shown in Fig. 11a and b, respectively. Loops form sequentially as the voids grow. The trailing partials are also formed and can be seen (arrows) in Fig. 11a-2 and b-3. In all cases the extremities of the dislocations remain attached to the void surface, and therefore no prismatic loops are observed. In Fig. 11a-3 and 4 the partial loops completely surround the voids.

The effect of void size on the stress required for loop emission was determined and compared to the analytical predictions of Lubarda et al. [19]. This analysis is two-dimensional and assumes a plane strain with far field stresses $\sigma_{xx} = \sigma_{yy}$. The corresponding von Mises stresses were calculated assuming a dislocation core radius equal to the Burgers vector b ($\rho = 1$). For the MD computation, the von Mises stress was calculated from the state of uniaxial strain. The results are shown in Fig. 12, in which the normalized von Mises stress (σ_{VM} divided by shear modulus G) is plotted against the normalized void radius (R divided

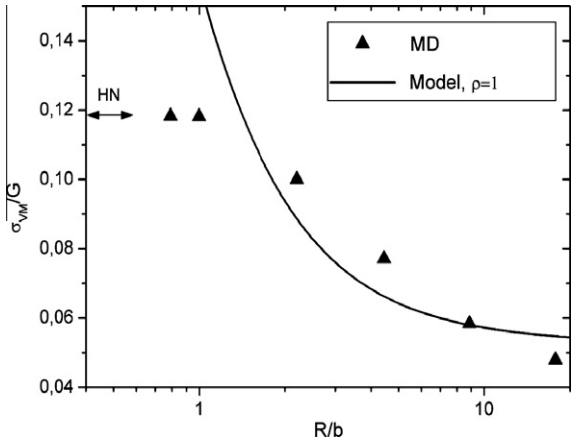

Fig. 12. Normalized von Mises stress for dislocation loop emission as a function of normalized void radius according to analytical model of Lubarda et al. [19] and from our molecular dynamics simulations using $G = 48$ GPa and $b = 0.255$ nm. MD calculations predict a maximum value of $\sigma_{vM}/G = 0.12$ whereas the model breaks down for $R/b < 1$. The region where homogeneous nucleation of dislocation loops occurs is marked "HN".

by the Burgers vector b). The Lubarda et al. [19] analysis compares well with the MD predictions for $R/b > 1$, i.e. for a void radius larger than the dislocation core radius. As expected, the model fails as the radius of the void goes to zero, and the stress calculated analytically goes to infinity. MD results approach the theoretical stress for homogeneous loop nucleation HN as R approaches zero.

An important question is: how does the detailed configuration of void surface affect the generation of defects? The surfaces of voids generated by MD were imaged and Fig. 13 shows their structures for different radii. Two observations can be made:

1. The sphericity of void diminishes as the void radius is decreased. For $R = 11$ nm (Fig. 13a), the void is fairly spherical; for $R = 0.5$ nm (Fig. 13e), it is clearly faceted. This deviation is even more pronounced if we look at the voids with radii $R = 0.3$, 0.2, 0.15 nm, formed by a few vacancies (Figs. 10 and 11). These voids are no longer spherical.
2. The surface atoms form steps that are one atomic size high. These can be seen as circles in Fig. 13a and b. The vector emanating from the center of the void and perpendicular to the plane of the paper is ⟨1 0 0⟩. The four other circle centers in Fig. 13a corresponds to the four ⟨1 1 1⟩ directions. These act as centers of circles with blue[1] atoms. They correspond to the steps.

In Fig. 13b, by virtue of the decrease in void size to $R = 5$ nm, the four lateral circles become hexagons (due to the symmetry of the {1 1 1} planes) while the central one becomes a square (due to the symmetry of the {1 0 0} planes). This effect accentuates itself as the void size decreases and the faceting leads to the classic "soccer ball" hexagon-square pattern. Fig. 13f shows the positions of the four {1 1 1} planes and ⟨1 0 0⟩ directions.

The steps along the surface have also been called ledges in the earlier literature and they are known to be favored sites for dislocation nucleation. Indeed, Li [61] was the first to point out their possible importance in the generation of dislocations. Murr [62] has an extensive treatment on ledges forming along grain boundaries. Ledges are also known to form at the interfaces of precipitates and matrix, as was demonstrated by Weatherly [63]. Thus, these ledges are thought to have a significant effect on the generation of dislocations, an effect not heretofore considered.

We are not aware of any discussion in the literature about steps on the void surface influencing dislocation nucleation during void growth, even when faceting was evident [24,31]. For cylindrical nanopillars, surface steps have been shown to control dislocation nucleation [64]. However, for "spherical" voids, the surface steps are only 1–2 a_0 long above $R \sim 2$ nm, and therefore this effect would not necessarily influence nucleation as much as in nanopillars, except for the fact that stress concentration is the leading cause for nucleation at the void surface.

Because our void surfaces do not contain the long edges of typical surface steps, or nanowires, we would benefit from studies of nucleation from nanoislands. Relatively little research exists in this area. The equilibrium shape and dislocation nucleation in strained epitaxial nanoislands discussed by Jalkanen et al. [65] considers only a particularly simple Lennard–Jones system. Note that islands in heteroepitaxial systems would be quite different due to strain gradients at the interface caused by the island and substrate being different materials.

It can be concluded that these surface steps can have an effect on the nucleation of dislocation loops. This effect has not been investigated in this context before.

3.3. Polycrystallinity effects

In order to investigate the effect of grain boundaries on void nucleation, Voronoi tesselation was used to generate a nanocrystalline structure with ~15 nm grain size. This grain size is located slightly above the Hall–Petch maximum and therefore most of the plastic activity is due to dislocations and not to grain boundary (GB) effects [58]. Results for plasticity induced by a pre-existing void at a single GB were presented by Traiviratana et al. [27], where emission of dislocations attached to the void surface lead to void growth and a region of significant plasticity around the void. Preliminary qualitative results for void nucleation in a nanocrystal under uniaxial tension were presented by Meyers et al. [66], who showed that for a nanocrystal under uniaxial tension several voids can nucleate and eventually coalesce, accompanied by plasticity. Rudd and Belak [29] also observed the formation of voids in nanocrystalline

[1] For interpretation of color in Figs. 2, 8, 13, 15, and 18, the reader is referred to the web version of this article.

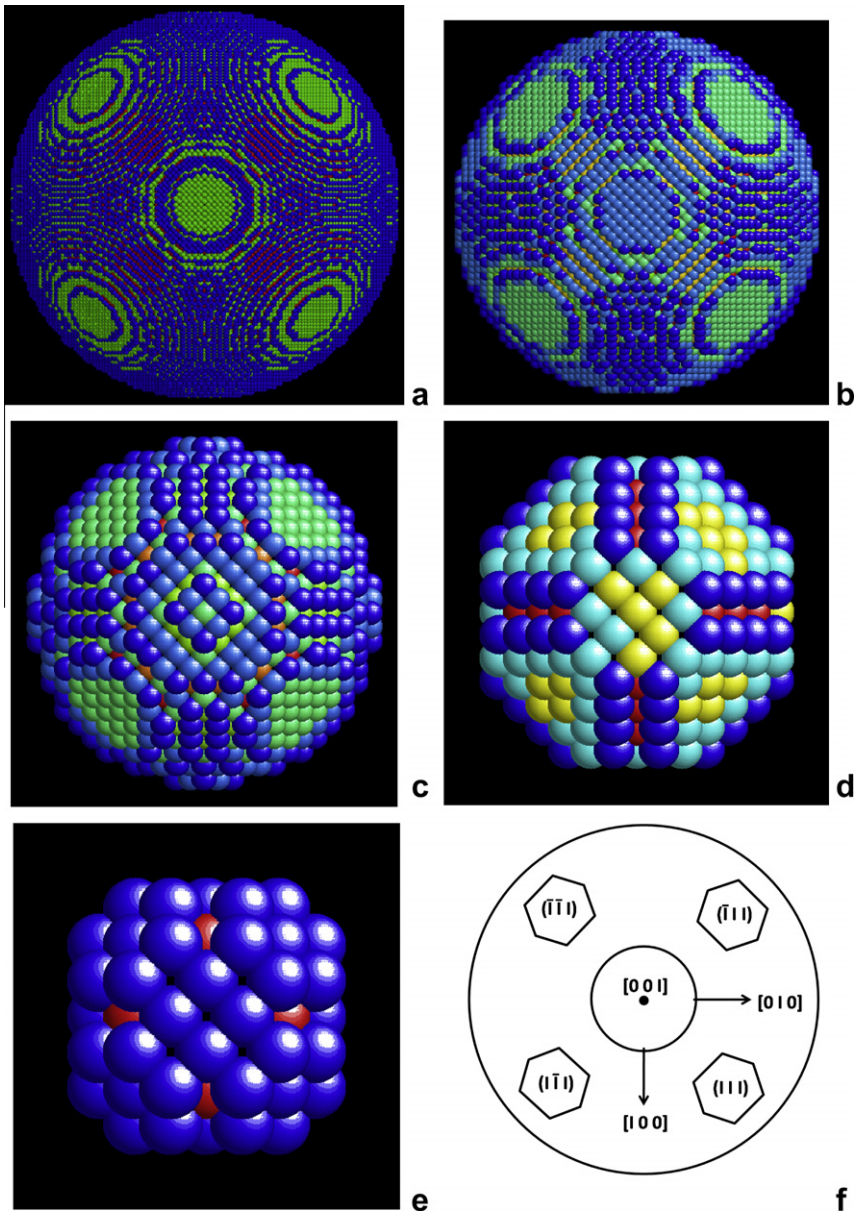

Fig. 13. Initial unrelaxed void surfaces colored according to a centrosymmetry parameter for: (a) $R = 11$ nm, (b) $R = 5$ nm, (c) $R = 2$ nm, (d) $R = 1$ nm and (e) $R = 0.5$ nm; (f) schematic of planes.

Cu, ~10 nm grain size, nucleated at GB junctions and growing along those GB, and commented on dislocation emission from the grain boundaries and void surfaces. Dongare et al. [44] have also shown void nucleation in a nanocrystal. They used 6 nm grains, where plastic activity would be dominated by GB sliding and emission of partial loops (e.g. [66]), and their initial simulation temperature is ~270 K, reaching more than 400 K at 15% strain. For uniaxial tension, they observe emission of partial dislocations from GB at ~6% strain, and nucleation of a single void at a mean stress ~10 GPa and von Mises stress ~1 GPa, slightly below 9% strain.

The hierarchy of void initiation sites is most clearly revealed in dynamic tensile straining (spalling) experiments, which produce strain rates on the order of $10^6\ s^{-1}$ and higher. In these experiments, the uniaxial strain state inhibits necking and the tensile instability responsible for the rupture fracture of aluminum observed by Chin et al. [2]. The flow stress is also raised by virtue of the effect of strain rate on the thermally activated dislocation motion. Thus, grain-boundary nucleation of voids becomes a prominent feature in polycrystalline fcc metals, as has been widely documented in the literature. A corollary of this is the interesting finding that polycrystalline copper exhibited a lower spall strength than monocrystalline copper. This was attributed to the existence of nucleation sites at grain boundaries in the polycrystals by Christy et al. [68] and Kanel et al. [69]. Meyers [70] also discusses this and provides an interpretation based on the greater availability of nucleation sites in the polycrystals. It should be

mentioned that, in the case of brittle particles bonded with the matrix, the stresses required for void formation increase with decreasing size, in a Hall–Petch-type manner.

For copper, the spall strength at high strain rates is on the order of few GPa, which is somewhat lower than the values predicted by MD [52]. In gas-gun experiments, the times at the tensile pulse are on the order of 10^{-6} s [72]. Schneider [73] reported a value of 5 GPa in laser compression experiments, in which the time was on the order of nanoseconds. Both values are considerably higher than the ones reported for gas-gun experiments [71].

The stresses required for growth of voids are indeed in the GPa range, according to the calculations. Armstrong [74] discusses this in the context of void initiation at the particle–matrix interface, and the Ritchie–Knott–Rice model [75] for ductile failure is based on the opening up of voids at spacings determined by second-phase particles.

3.3.1. Uniaxial strain loading

Figs. 14a–d show the evolution of voids in the nanocrystalline Cu specimen subjected to tension in uniaxial strain. The direction of loading is shown in Fig. 14a. Only the atoms on the surface of the voids are imaged. It can be seen that the voids, which are initially equiaxed, evolve by coalescence and develop elongated "sausage"-like shapes, as opposed to the more spherical shape seen for smaller grain size by Dongare et al. [44]. Cuts were made parallel to the tensile Z-axis and the sequence is shown in Fig. 15. As the stress is increased, partial dislocations and full dislocations are emitted from the grain boundaries. This is shown by light blue lines traversing the grains and is the classic mechanism of plastic deformation first identified by Van Swygenhoven and Caro [76] and later by others (e.g. [77–79]). One can see the advance of the leading and trailing partials in the bottom right-hand side of Fig. 15a and b, indicating full dislocation emission. The emission of dislocation loops from the grain boundaries leads to the nucleation of a void (marked by an arrow in Fig 15b). Upon increased loading, this void grows, while other two dislocations nucleate along the same boundary (Fig. 15c). In Fig. 15d two voids have already coalesced and there is a ligament separating the third, which is already ruptured in

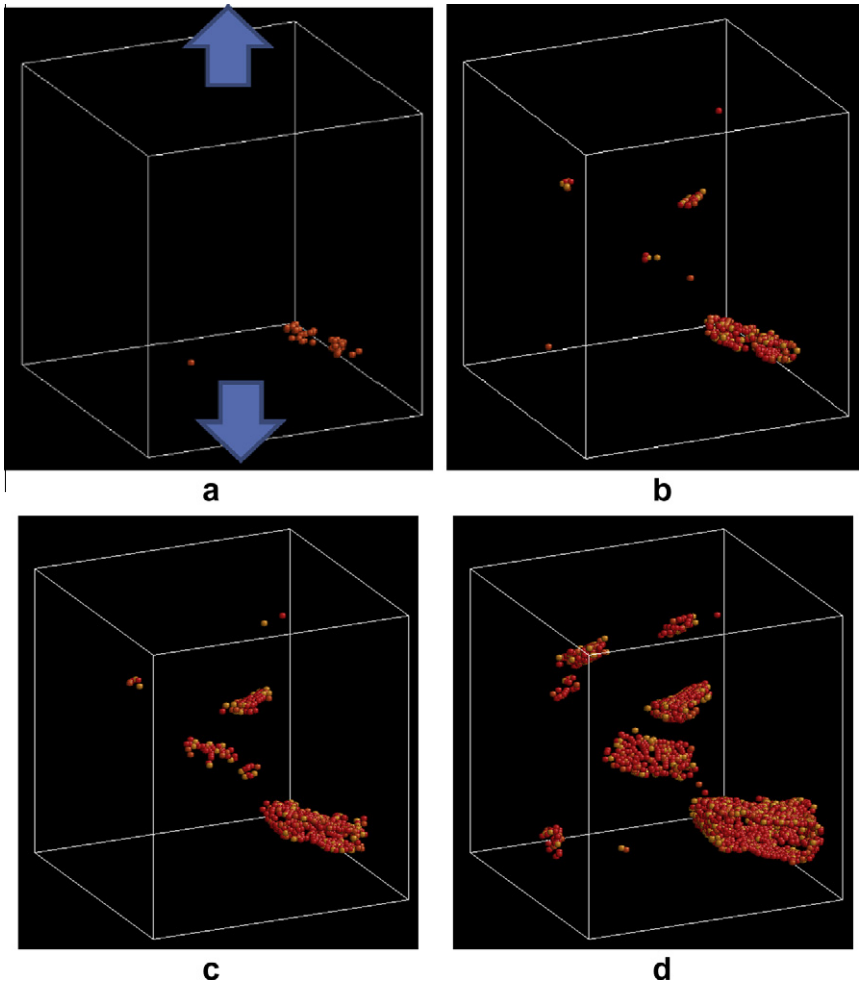

Fig. 14. Void initiation and propagation in nanocrystalline metal during uniaxial strain loading (the traction direction is marked in (a)); only atoms at free surfaces are shown. Strains are: (a) 6.5%; (b) 7%; (c) 7.3%; (d) 8%. Voids form at grain boundaries and grow preferentially along them. Note the coalescence events from (a) to (b), and from (c) to (d).

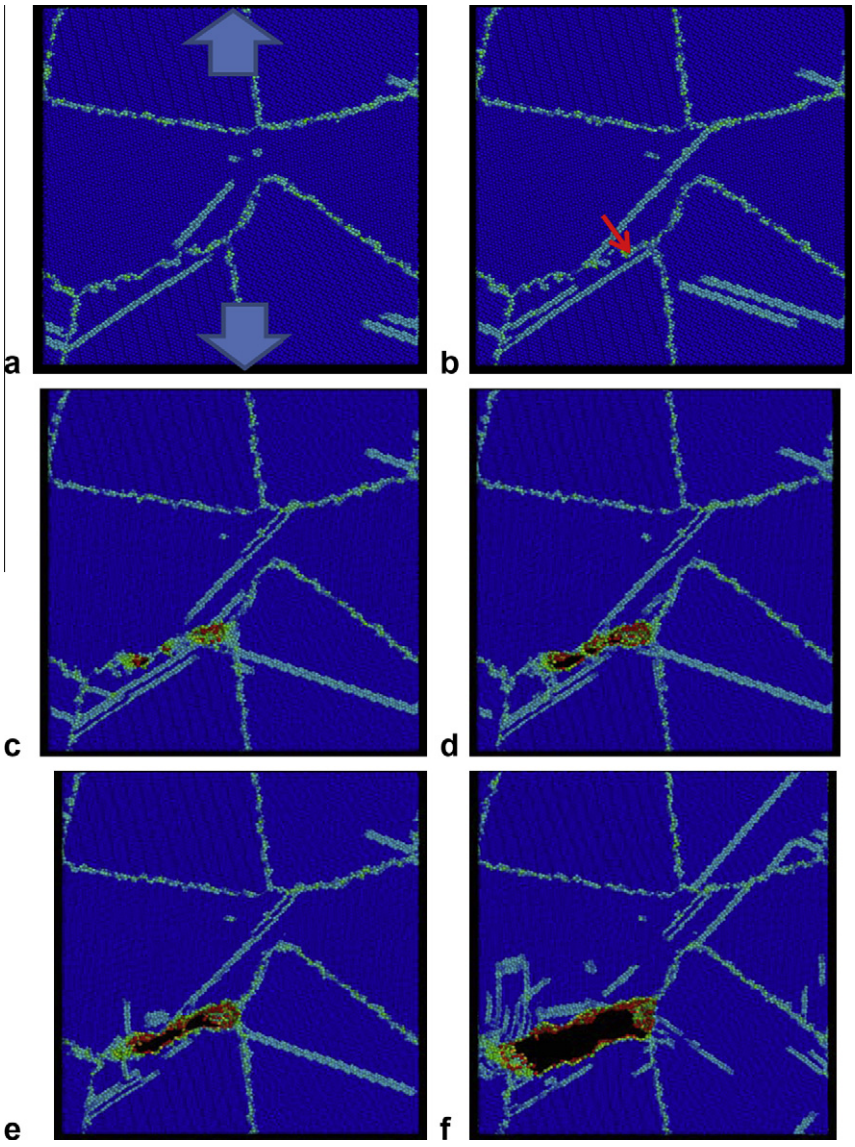

Fig. 15. Slices (a_0 thick) of the nanocrystalline sample under uniaxial tension. Strains are: 6%, 6.5%, 7%, 7.2%, 7.3% and 8%. Lattice atoms: blue; void surface atoms: red/green; stacking faults, partial dislocations and twin boundary atoms: light blue. Stacking faults show as two planes of atoms while twin boundaries show as a single atomic plane. (a) Emission of partial dislocations from GBs; (b) void nucleation (marked by an arrow); (c) three voids nucleated at a grain boundary; (d) coalescence of voids; (e and f) void opening by continued dislocation emission at its extremities. A few twin boundaries are seen in frames (c) and (d).

Fig. 15e. It is interesting to notice that the breaking of these ligaments does not require significant dislocation emission but takes place primarily by elastic stress release. In Fig. 15f the void has an elongated appearance, and its further growth is occurring at the left-hand side by profuse dislocation emission, in a mode akin to Rice's [80] mechanism for crack growth and observed for crack evolution in nanocrystalline metals [45,46,52]. This process was also modeled by Zhu et al. [81], who showed that curved loops form at the crack tip. This is a classical problem in fracture mechanics: the blunting of the crack tip is produced by shear (semi-) loop emission, which carries the material and opens up the space between by crack faces. There has been considerable experimental research on the growth and blunting of cracks. Jagannadham et al. [82] showed that dislocation emission from the surface of the crack creates ledge steps that blunt the crack. Vecchio and Hertzberg [83] proposed that in pure metals voids initiate and grow along dislocation cell walls formed during plastic deformation. In situ transmission electron microscopy was also conducted by Wilsdorf and co-workers [84–86]. However, this work failed to reveal the detailed nature of void growth.

The stress components, mean stress (pressure) and von Mises stress are plotted as functions of distension in Fig. 16. The uniaxial stress, σ_{zz}, is similar to that found for 12 nm nanocrystalline Ni [36] using stress-free conditions perpendicular to loading. However, there are several

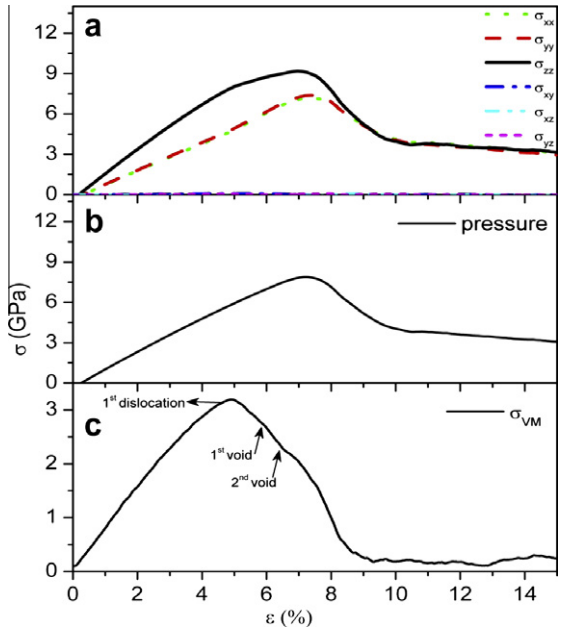

Fig. 16. Average stresses vs. strain for uniaxial strain loading of a nanocrystalline specimen; (a) six stress components; (b) hydrostatic stress; (c) von Mises stress.

differences with the single-crystal results presented in Fig. 7, and with the 6 nm nanocrystalline Cu results of Dongare et al. [44]. Linearity in the nanocrystalline case is lost earlier than in the monocrystalline case because of GB sliding and later (4.7% strain) dislocations emitted from the GBs. The void nucleates and starts growing at ~5.9% strain, at a von Mises stress of ~2.3 GPa = 0.05G. This relatively low value is expected due to the existence of grain-boundary and triple-point sites. This stress can be compared to the von Mises stress for void growth of the smallest void considered in the previous section, which was ~0.12G. This value is roughly equivalent to the von Mises stress for void growth for an ~4 nm radius void in a single crystal loaded along [0 0 1]. There could many reasons why the stress found here is higher than that found in Ref. [44]; for instance, Dongare et al. used a different EAM potential, the Voter–Chen Cu potential [67]. In addition, it would be expected that, for a given set of grain orientations, the "weakest" GB would fail first. Given computational constrains for simulations with large grains (15 nm grains), we have fewer grains than [44] (6 nm grains), and therefore our set of GBs might not include some of the weakest GB types. Simulations with ~10^8 atoms would be needed to include a large number of GBs and to obtain a better estimate for the von Mises stress for void nucleation. Despite this caveat, we have enough GBs to capture the general behavior of large grains. Because dislocation activity is much more likely than in small grains, (i) the stress drop after void nucleation is not precipitous, as seen in Fig. 7 and Ref. [44]; (ii) dislocation activity, including twin formation, continues without the need to form an amorphous plastically deformed region around the void; and (iii) other voids are nucleated along the same GB and eventually coalesce.

3.3.2. Hydrostatic loading

The hydrostatic expansion of the nanocrystalline sample was also modeled. Fig. 17a–d shows the evolution of voids in the nanocrystalline Cu specimen subjected to hydrostatic strain. As in Fig. 14, only the atoms on the surface of the voids are imaged. Multiple voids nucleate under loading, and their evolution is analogous to the one in uniaxial strain loading. Voids appear at lower strains, around 3.5% vs. 6%, and end up coalescing into a single large void. However, volumetric strain at nucleation for hydrostatic loading is larger than for uniaxial loading. Cuts were made parallel to the tensile Z-axis and the sequence is shown in Fig. 18, which shows the sequence of events for strains of 3.58%, 3.6%, 3.61%, 3.66%, 3.78% and 4.66%. Fig. 18a shows one dislocation emitted from a boundary. It is marked by an arrow. At the approximate position where the dislocation originated, two voids start to form in Fig. 18b. The ligament between voids is broken (Fig. 18c and d) and a new void is nucleated along the same GB. The nucleation of an additional void is shown in Fig. 18e, which also joins the main void by the last frame shown here (Fig. 18f). Note the nucleation and later closure

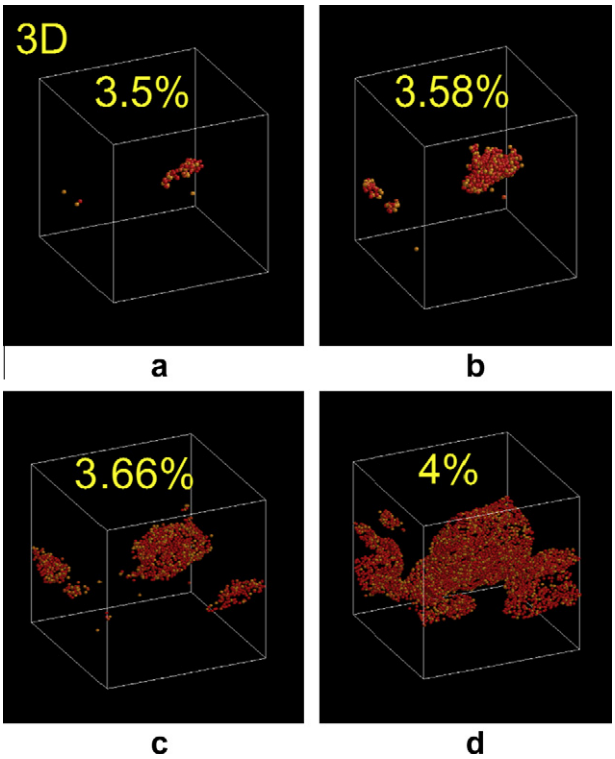

Fig. 17. Void initiation and propagation in nanocrystalline copper in hydrostatic loading; only atoms on the void surfaces are visible. Strains: (a) 3.5%; (b) 3.58%; (c) 3.66%; (d) 4%. Voids form at grain boundaries and grow preferentially along them. At the end of our simulation, there is only a single void when one considers periodic simulation boundaries. Note the coalescence event from (a) to (b) and from (c) to (d).

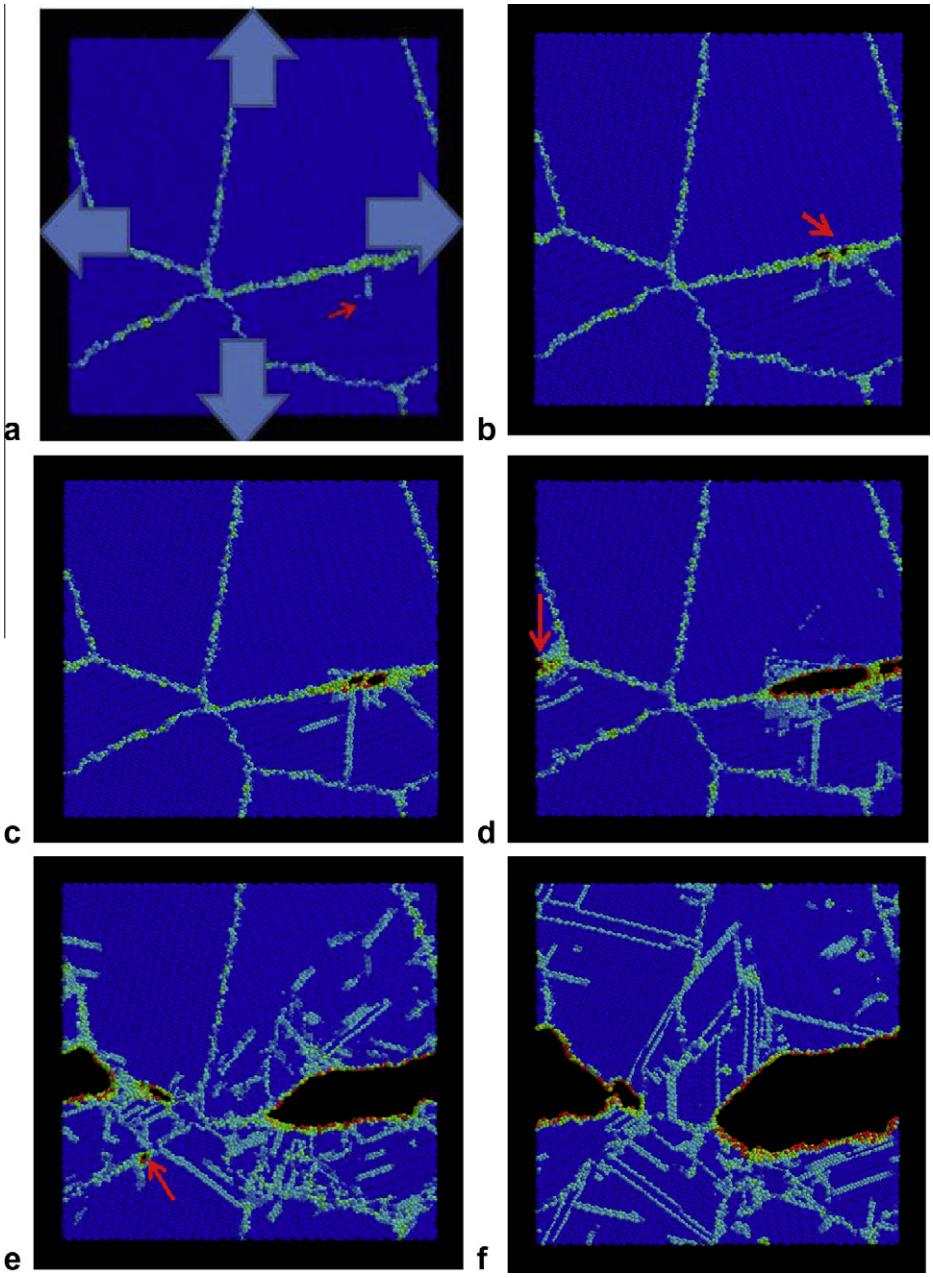

Fig. 18. Slices (a_0 thick) of the nanocrystalline sample under hydrostatic tension. Strains are: 3.58%, 3.6%, 3.61%, 3.66%, 3.78% and 4.66%. Lattice atoms: blue; void surface atoms: red/green; stacking faults, partial dislocations and twin boundary atoms: light blue. Stacking faults show as two planes of atoms, while twin boundaries show as a single atomic plane. (a) Emission of partial dislocations from GBs; (b) void nucleation (marked by an arrow); (c and d) continued void growth along grain boundary, with void nucleation marked by an arrow; (e and f) void opening by continued dislocation emission at their extremities, leading eventually to coalescence. A large number of twin boundaries are seen in the last frame.

of a small void at a GB in the lower left corner (Fig. 18e, arrow).

Thus, the process of void nucleation, growth and coalescence along the grain boundaries is similar to the one for uniaxial strain loading. However, there are significant differences in the stresses at which these events occur, as is clear by comparing Figs. 16 and 19. First, the maximum pressure is considerably higher for the hydrostatic loading case: 12 GPa vs. 8 GPa. The von Mises stress, which represents an average of all the atoms in the computation box, has quite different trajectories, as expected: it rises to ~3 GPa for uniaxial strain loading but only to ~1.5 GPa for the hydrostatic loading. The strains for the emission of the first partial and for the initiation of voids are also marked in Figs. 16c and 19c. In uniaxial strain, the first void forms at a strain of ~6%. For the hydrostatic case, this strain is ~3.5%.

3.3.3. Defect and temperature evolution

The formation of dislocations and the opening of voids were quantified by computing the evolution of three parameters: atoms on void surfaces, at the leading and

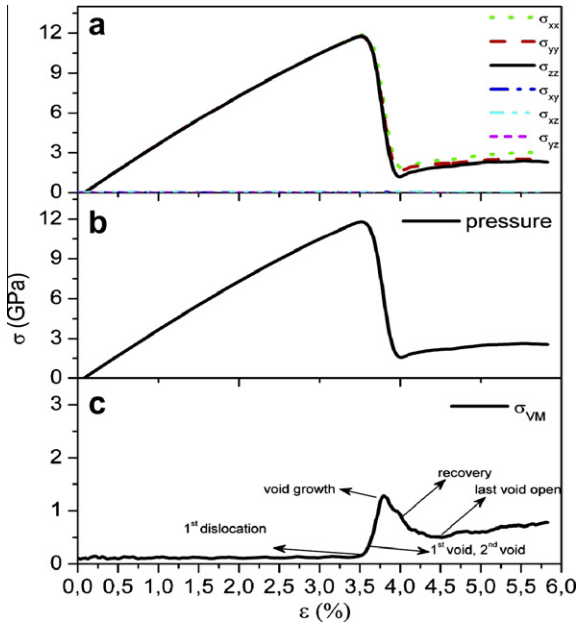

Fig. 19. Average stresses vs. strain for the hydrostatic loading of nanocrystalline specimen: (a) six stress components; (b) hydrostatic stress; (c) von Mises stress.

trailing partial dislocation lines, and in the stacking faults. These three parameters describe the evolution of damage and plastic deformation very well, as can be seen from Fig. 20, where the number of atoms in defects is plotted vs. strain for both hydrostatic and uniaxial strain loading. Partial dislocations, stacking faults and the free surfaces of the voids were selected by CSP filtering. The number of atoms in grain boundaries was assumed to be constant and was subtracted. The number of atoms in partial dislocations, N_p, allows an approximate calculation of dislocation density, ρ, through [87,88]:

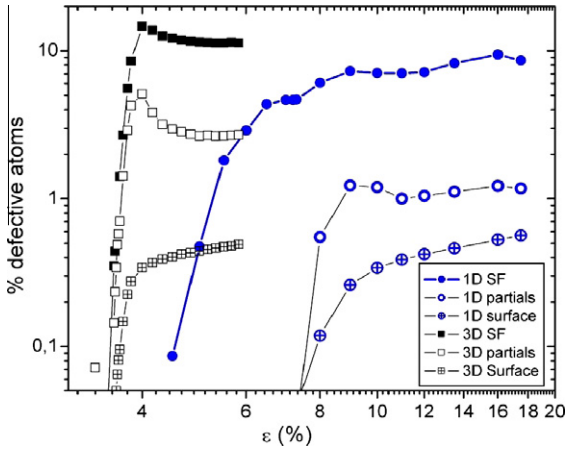

Fig. 20. Percentage of defective atoms as a function of strain for uniaxial strain (1-D) and hydrostatic (3-D) loading of a nanocrystalline specimen. Surface atoms represent opening of voids; partials represent only atoms along the leading and trailing dislocation lines; SF represents all atoms on stacking fault ribbons.

$$\rho = (1/2)(N_p d)/Volume$$

where $d \sim 0.25$ nm for Cu is the distance between atoms along a dislocation line. The factor (1/2) takes into account that there are two planes on each partial dislocation as seen by CSP filtering, but only one dislocation line. For uniaxial strain, final values are: $\rho \sim 10^{13}\,\mathrm{cm}^{-2}$. For hydrostatic loading, $\rho \sim 2 \times 10^{13}\,\mathrm{cm}^{-2}$, which is similar to the values found in shocked single crystals [87,88,91] and nanocrystals [89,90] during loading. Of course, dislocation densities in recovered, unloaded, experimental samples are significantly smaller, as expected [88,89].

Fig. 20 shows that the three parameters rise rapidly and then reach a plateau. For hydrostatic loading, the critical strain for dislocation emission and void opening is lower than for uniaxial strain, as was seen earlier by comparing Figs. 16 and 19. For the hydrostatic case, recovery dominates after 4%, with the disappearance of stacking faults and twin formation, but, starting at ~5%, there is a combination of recovery and creation of new dislocations. The

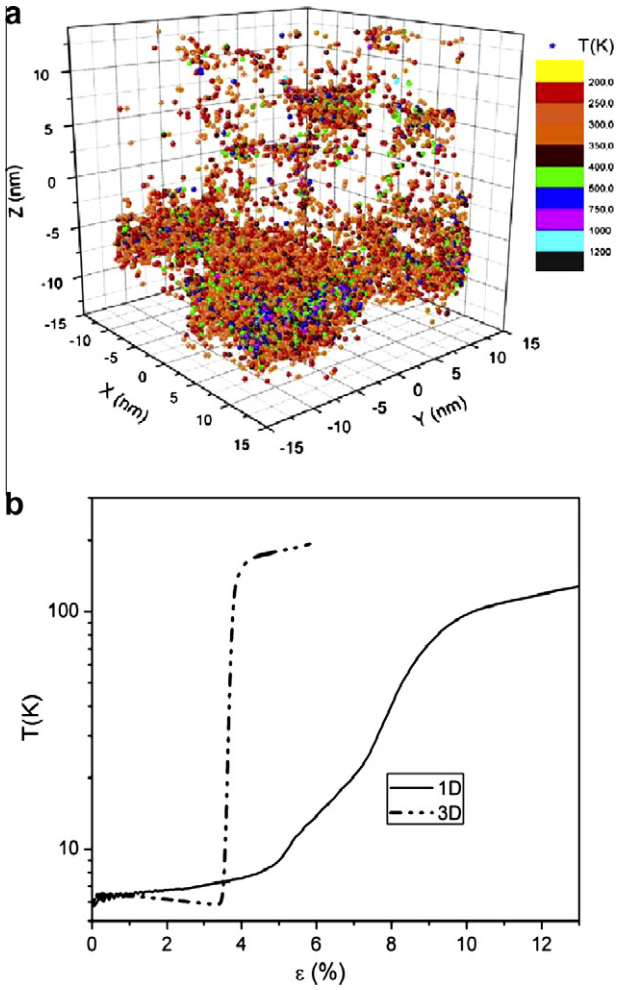

Fig. 21. (a) Snapshot of a nanocrystalline specimen at 9% strain (uniaxial strain), showing only atoms with "atomic temperature" $T > 200$ K, for a temperature of 170 K for the whole sample; (b) plot of temperature vs. strain for uniaxial strain (1-D) and hydrostatic (3-D) loading.

increase in void volume continues during this recovery stage. For the uniaxial strain case, recovery is less prominent.

The presence of grain boundaries thus has a profound effect on the generation of voids and on the stress at which dislocation emission takes place, but does not affect the basic picture where shear loop emission helps void growth at grain sizes above the Hall–Petch maximum. The preferential propagation of failure along the grain boundaries will lead to shallow dimples. Indeed, these shallow dimples have been observed in nanocrystalline nickel [92,93].

The temperature evolution inside of the nanocrystalline specimens as a function of plastic strain was estimated by calculating an "effective" atomic temperature T for each atom, assuming it to be proportional to its kinetic energy (KE), $KE = (3/2)k_BT$, where k_B is the Boltzmann constant. The highest T is reached around the voids. Fig. 21a shows only atoms with "effective temperature" $T > 200$ K for a temperature of 70 K for the whole sample subjected to uniaxial strain loading to a plastic strain of 9%. This corresponds, in Fig. 15, to a strain slightly higher than the one in Fig. 15f. The different temperatures are coded with different colors. It is clear that the temperature distribution is highly non-uniform and that the void surfaces are much hotter than the regions far from them. This is a direct result of the localized plastic deformation. Fig. 21b compares the average temperature evolution for the uniaxial strain (1-D) and hydrostatic tension (3-D) cases. As shown in Sections 3.3.1 and 3.3.2, the strain for the initiation of void formation is lower for the hydrostatic case, and this is reflected in the plot. The temperature rises, which start at 3.5% and 6.5%, respectively, for the two cases, are consistent with void initiation and growth. However, these average temperature values do not reflect the situation in the sample being deformed, and one can even envisage regions with localized melting and amorphization, as in Ref. [44], where the average temperature reached 400 K and an amorphous region surrounded the deformed void.

4. Conclusions

1. The mechanism of void nucleation and growth by the cooperative emission and expansion of dislocation loops which nucleate at the void surface is confirmed by our molecular dynamic simulations for three loading orientations: [1 0 0], [1 1 0] and [1 1 1]. The extremities of the loops remain attached to the void surface, since their detachment would nullify the volume increase of the void. A complete loop is volume invariant and produces only shear in the region bounded by the dislocation.
2. Loop formation proceeds by the emission of a partial dislocation at a slip plane oriented for maximum shear stress. The loop configuration is dependent on the orientation of the tensile axis, which dictates the number and orientation of the slip systems with the maximum Schmid factor. For [1 1 0] loading, only monoplanar loops were observed; for [1 0 0], biplanar loops were seen, and for [1 1 1], triplanar loops.
3. The mechanisms of reaction for triplanar loops are analyzed and it is shown that the leading partial dislocations react along the intersecting slip planes, creating sessile dislocations. These are cancelled by the trailing partial dislocations. It is shown that the trailing partials have to remain attached to the void surface to ensure slip along two directions on the same plane – an apparent paradox.
4. While the calculations were carried out for a void with 2 nm radius, the same mechanism operates for larger and smaller voids, with radius as low as 0.15 nm (containing two vacancies). Convergent vacancy diffusion is not required for void formation, and the calculations presented here confirm a dislocation-based mechanism for void growth consistent with the shear loops postulated by Ashby [20,21] for inhomogeneous plastic deformation, illustrated by rigid inclusions.
5. The velocities of the leading partials were estimated from the loop expansion and found to be of the order of 1000 m s^{-1}. These velocities are compared with the ones extracted from earlier MD simulations on the collapse of voids [26]. These latter results indicate supersonic partial dislocations, if the stress is sufficiently high. These results agree with those of Germann et al. [94], who found that the leading partials could travel subsonically or supersonically, depending on the shock stress for shock propagation along [1 0 0].
6. The nucleation of voids in a nanocrystalline sample takes place along the grain boundaries. Voids grow and coalesce along the boundaries, and less dislocation emission is required since the opening loses its equiaxed nature and becomes elongated, acting as a crack.
7. The initiation of voids in uniaxial strain and hydrostatic loading was compared and no significant difference was found in the mechanisms; however, the von Mises stress evolution depends on the stress/strain state. Void initiation occurs at significantly lower strains for hydrostatic loading.
8. It is proposed that void initiation in metals takes place in a hierarchy of sites, starting, at the lowest stress level, with large inclusions and other imperfections such as the interface of dispersed phases, and proceeding, at increasing stress levels, to grain boundaries and grain junctions, and, at even higher stresses, to larger vacancy complexes, and finally to divacancies. It is also proposed that, for nanosized voids and grain-boundary sites, dislocation loop emission is the principal agent of outward matter transport under most conditions.
9. Our simulations will hopefully help to calibrate models at larger scales [95–98], including finite element model calculations of void growth/collapse.

10. The voids are not perfect spheres but have steps that have a height of approximately one lattice spacing. As the void size decreases, the shape departs from sphericity. The steps most likely have an effect through the nucleation of shear loops, in a manner akin to the nucleation of dislocations at grain-boundary ledges, interfaces and free surface steps.

Acknowledgements

Financial support from LLNL Grant B558558, ILSA Contract Number W-7405-Eng-48 (program manager: Dr D. Correll) and the UCRL program is gratefully acknowledged. Discussions with Prof. V.A. Lubarda about dislocation reactions are gratefully acknowledged. We thank allocations at the San Diego and Texas Supercomputer Centers through Teragrid and Chia-Hui Lu for help with manuscript.

References

[1] Tipper CF. Metallurgia 1949;39:133.
[2] Chin GY, Hosford WF, Backofen WA. Trans Metall Soc AIME 1964;230:437–49.
[3] Rosi FD, Abrahams MS. Acta Metall 1960;8:807–8.
[4] Needleman A. J Appl Mech 1972;39:964–70.
[5] Koplik J, Needleman A. Int J Solids Struct 1988;24:835–53.
[6] Tvergaard V, Hutchinson JW. J Mech Phys Solids 1992;40:1377–97.
[7] Pardoen T, Hutchinson JW. J Mech Phys Solids 2000;48:2467–512.
[8] Gurson AL. J Eng Mater Technol 1977;99:2–15.
[9] McClintock FA. J Appl Mech 1968:363–71.
[10] Dodd B, Bai Y. Ductile fracture and ductility. New York: Academic Press; 1987. p. 97.
[11] Cuitiño AM, Ortiz M. Acta Mater 1996;44:427.
[12] Surholt T, Herzig C. Acta Metall 1997;45:3817.
[13] Raj R, Ashby MF. Acta Metall 1975;23:653.
[14] Stevens AL, Davison L, Warren WE. J Appl Phys 1972;43:4922.
[15] Meyers MA, Aimone CT. Prog Mater Sci 1983;28:1.
[16] Broek D. Elementary engineering fracture mechanics. 4th ed. Dordrecht: Martinus Nijhoff; 1986. p. 56.
[17] Wolfer WG. Philos Mag A 1988;48:285.
[18] Ahn DC, Sofronis P, Kumar M, Belak J, Minich RJ. Appl Phys 2007;101:063514-1-6.
[19] Lubarda VA, Schneider MS, Kalantar DH, Remington BA, Meyers MA. Acta Mater 2004;53:1397.
[20] Ashby MF. Philos Mag 1970;21:399.
[21] Ashby MF. In: Kelly A, Nicholson RB, editors. Strengthening methods in crystals. Amsterdam: Elsevier; 1971. p. 37.
[22] Traiviratana S, Bringa EM, Benson DH, Meyers MA. Acta Mater 2008;56:3874.
[23] Meyers MA, Traiviratana S, Lubarda VA, Benson DJ, Bringa EM. J Mater 2009;61:35.
[24] Marian J, Knap J, Ortiz M. Phys Rev Lett 2004;93:1.
[25] Marian J, Knap J, Ortiz M. Acta Mater 2005;53:2893.
[26] Dávila LP, Erhart P, Bringa EM, Meyers MA, Lubarda VA, Schneider MS, et al. Appl Phys Lett 2005;86:161902.
[27] Zhu W, Song Z, Deng X, He H, Cheng X. Phys Rev B 2007;75:0241014-1.
[28] Marian J, Knap J, Campbell GH. Acta Mater 2008;56:2389–99.
[29] Rudd RE, Belak JF. Comput Mater Sci 2002;24:148.
[30] Seppälä ET, Belak JF, Rudd RE. Phys Rev B 2004;69. 134101-1-19.
[31] Seppälä ET, Belak JF, Rudd RE. Phys Rev Lett 2004;93:245503-1-4.
[32] Seppälä ET, Belak JF, Rudd RE. Phys Rev B 2005;71. 064112-1-10.
[33] Srinivasan SG, Baskes MI, Wagner GJ. J Mater Sci 2006;41:7838.
[34] Potirniche GP, Horstemeyer MF, Wagner GJ, Gullett PM. Int J Plast 2006;22:257.
[35] Rudd RE. Philos Mag 2009;89:3133–61.
[36] Zhao KT, Chen CQ, Shen YP, Lu TJ. Comput Mater Sci 2009;46:749–54.
[37] Seitz F. Phys Rev 1950;79:723.
[38] Brown LM. Philos Mag 1970;21:329.
[39] Hirsch PB. J Inst Metals 1957;86:13.
[40] Hirsch PB. In: Thomas G, Fulrath RM, Fischer RM, editors. Electron microscopy and structure of materials. CA: University of California Press; 1972.
[41] Silcox J, Hirsch PB. Philos Mag 1958;4:72.
[42] Humphreys FJ, Hirsch PB. Proc Roy Soc Lond 1970;318:73.
[43] Uberuaga BP, Hoagland RG, Voter AF, Valone SM. Phys Rev Lett 2007;99:135501.
[44] Dongare AM, Rajendran AM, LaMattina B, Zikry MA, Brenner DW. Phys Rev B 2009;80:104108.
[45] Farkas D, Van Petegem S, Derlet P, Van Swygenhoven H. Acta Mater 2005;53:3115–23.
[46] Cao A, Wei Y. Phys Rev B 2007;76:024113.
[47] Plimpton SJ. J Comput Phys 1995;117:1.
[48] Daw MS, Baskes MI. Phys Rev B 1984;29:6443.
[49] Mishin T, Mehl MJ, Papaconstantopoulos DA, Voter AF, Kress JD. Phys Rev B 2001;63:1.
[50] Kelchner CL, Plimpton SJ, Hamilton JC. Phys Rev B 1998;58:11085.
[51] Minich RW, Cazamias JU, Kumar M, Schwartz AJ. Metall Mater Trans A 2004;35A:2663.
[52] Luo S-N, An Q, Germann TC, Han L-B. J Appl Phys 2009;106:013502.
[53] Frank FC. Proc Phys Soc A 1949;62:131.
[54] Eshelby JD. Proc Phys Soc A 1949;62:307.
[55] Weertman J. In: Shewmon PG, Zackay VF, editors. Response of metals to high-velocity deformation AIME. New York: Interscience; 1961. p. 205.
[56] Weertman J, Weertman JR. In: Nabarro FRN, editor. Dislocations in solids. Amsterdams: North-Holland Publishing; 1980. p. 1–59.
[57] Gumbsch P, Gao HJ. Science 1999;283:965.
[58] Tsuzuki H, Brenicio PS, Rino JP. Appl Phys Lett 2008;92:191909.
[59] Bringa EM. J Appl Phys 2004;96:3793.
[60] Bringa EM, Caro A, Wang YM, Victoria M, McNaney JM, Remington BA, et al. Science 2005;309:1838–41.
[61] Li JCM. Trans TMS-AIME 1963;227:239.
[62] Murr LE. Interfacial phenomena in metals reading. MA: Addison-Wesley; 1975. p. 255.
[63] Weatherly GC. Acta Metall 1971;19:181–92.
[64] Zepeda-Ruiz LA, Sadigh B, Biener J, Hodge AM, Hamza AV. Appl Phys Lett 2007;91:101907.
[65] Jalkanen J, Rossi G, Trushin O, Granato E, Ala-Nissila T, Ying SC. Phys Rev B 2010;81:041412.
[66] Meyers MA, Mishra A, Benson DJ. Prog Mater Sci 2006;51:427.
[67] Voter AF. In: Westbrook JH, Fleisher RL, editors. Intermetallic compounds: principles and practice, vol. 77. New York: Wiley; 1994.
[68] Christy S, Pak Hr, Meyers MA. Metallurgical applications of shock-wave and high-strain rate phenomena. New York: Marcel Dekker; 1991. p. 775.
[69] Kanel GI, Rasorenov SV, Fortov VE. Shock-wave and high-strain rate phenomena in materials. New York: Marcel Dekker; 1991. p. 775.
[70] Meyers MA. In: Meyers MA, Armstrong RW, Kirchner HOK, editors. Mechanics and materials: fundamentals and linkages. New York: Wiley; 1999. p. 489–594.
[71] Grady DE. J Mech Phys Solids 1988;36:353.
[72] Moshe E, Eliezer S, Deckel E, Ludminsky A, Henis Z, Goldberg IB, et al. J Appl Phys 1998;83:4004.
[73] Schneider MS. Doctoral dissertation. San Diego: University of California; 2004.
[74] Armstrong RW. In: Meyers MA, Armstrong RW, Kirchner HOK, editors. Mechanics and materials: fundamentals and linkages. New York: Wiley; 1999. p. 363–98.

[75] Ritchie RO, Knott JF, Rice JR. J Mech Phys Solids 1973;21:395–410.
[76] Van Swygenhoven H, Caro A. Appl Phys Lett 1997;71:1652.
[77] Froseth AG, Derlet PM, Van Swygenhoven H. Acta Mater 2004;52:5870.
[78] Yamakov V, Wold D, Phillpot SR, Gleiter H. Acta Mater 2002;50:5005.
[79] Schiøtz J, Jacobsen KW. Science 2003;301:1357.
[80] Rice JR. J Mech Phys Solids 1992;40:239.
[81] Zhu T, Li J, Yip S. Phys Rev Lett 2004;93:025503:1-4.
[82] Jagannadham K, Wilsdorf HGF, Weertman J. Mater Res Innovat 1998;1:254–64.
[83] Vecchio KS, Hertzberg RW. J Mater Sci 1988;23:2220–4.
[84] Lyles RL, Wilsdorf HGF. Acta Metall 1975;23:269–77.
[85] Chan IYT, Wilsdorf HGF. Mater Sci Eng 1981;49:229–77.
[86] Pollock TC, Wilsdorf HGF. Mater Sci Eng 1983;61:7–15.
[87] Liu W, Zhang X, Tang J. Mech Mater 2009;41:799–809.
[88] Cao BY, Bringa EM, Meyers MA. Metall Mater Trans 2007;38A:2681–8.
[89] Jarmakani HN, Bringa EM, Erhart P, Remington BA, Wang YM, Vo NQ, et al. Acta Mater 2008;56:5584.
[90] Bringa EM, Rosolankova K, Rudd RE, Remington BA, Wark JS, Duchaineau M, et al. Nature Mater 2006;5:805.
[91] Shehadeh MA, Bringa EM, Zbib HM, McNaney JM, Remington BA. Appl Phys Lett 2006;89:171918.
[92] Kumar KS, Suresh S, Chrsholm MF, Horton JA, Wang P. Acta Mater 2003;51:387.
[93] Hasnaoui A, Van Swygenhoven H, Derlet PM. Science 2003;300:1550.
[94] Germann TC, Tanguy D, Holian BL, Lomdahl PS, Mareschal M, Ravelo R. Metall Mater Trans 2004;35A:2609–15.
[95] Barton DC, Waheed M, Mirza MS, Church E. Int J Fract 1995;73:325–43.
[96] Horstemeyer MF, Matalanis MM, Sieber AM, Botos ML. Int J Plast 2000;16:979–1015.
[97] Liu WH, Zhang XM, Tang JG, Du YX. Comput Mater Sci 2007;40:130–9.
[98] Wen ZX, Yue ZF. Comput Mater Sci 2007;40:140–6.